Galaxy flows in cosmic filaments

Master's thesis
University of Turku
Astronomy
2021
B.Sc. Suvi Korhonen
Examiners:
Dr. Pekka Heinämäki
Prof. Seppo Mattila

The originality of this thesis has been checked in accordance with the University of Turku quality assurance system using Turnitin Originality Check service.

UNIVERSITY OF TURKU
Department of Physics and Astronomy

Korhonen, Suvi Galaxy flows in cosmic filaments

Master's thesis, 68 pp.
Astronomy
July 2021

In the universe galaxies are assembled into the cosmic web, consisting of voids, walls, galaxy clusters and filaments. Filaments are elongated matter flows connecting the clusters together. Because of the non-uniform matter distribution in the universe, galaxies acquire peculiar velocities deviating from the expansion velocity of the universe. These peculiar motions trace the formation history of the cosmic web.

This thesis studies the effect of the filament environment on the peculiar motions of central galaxies using the hydrodynamical EAGLE simulation and filaments identified with the Bisous method. The magnitude of the galaxy peculiar velocity and the alignment angle between the peculiar velocity vector and the filament spine are measured. The peculiar motions inside and outside of filaments are compared and measured with fixed geometric properties of filaments and baryonic properties of galaxies. The analysis is done with fixed group mass to avoid the effect of the local environment on the peculiar motions.

The analysis reveals that the central galaxies move more slowly and more parallel to the filament spines inside of filaments than on the outside. The peculiar velocities increase and motions become more parallel in the shortest and longest filaments. In the direction parallel with the filament spines, the alignment of motions of central galaxies in low mass groups indicate that filaments transport galaxies into clusters. Perpendicular to the filament spines, the peculiar velocities of central galaxies in low mass groups are the highest near the filament edges and decrease on both sides. Massive groups are found to concentrate in short filaments and near the filament spines. The central galaxies in the massive groups have the most parallel motions, both inside and outside of filaments. In general, the peculiar motions depend on the group mass, velocities decreasing with increasing group mass. The baryonic properties of galaxies are found to have no effect on the peculiar motions.

Together the results hint that in the parallel direction the peculiar motions are the most affected by the clusters connected to the filaments, while the galaxy number densities within filaments determine the motions in the perpendicular direction. This thesis broadens the view on how the filament environment affects the flows of galaxies.

Keywords: peculiar motions, filaments, large-scale structure, simulations

Contents

Introduction

The galaxies in the universe are not randomly distributed, but are woven together forming a foam like structure, the cosmic web. The cosmic web contains void regions nearly empty of galaxies, thin wall like structures, galaxy clusters and filaments. Filaments are long elongated matter flows, binding the web together. The local, group environment is known to have an effect on the evolution of galaxies, seen in properties such as mass and star formation rate. Yet, the effect of the large-scale environment on the galaxy evolution is not fully understood.

The cosmic web has formed under the laws of gravity in the universe that has been expanding since the cosmic dawn. Galaxies acquire motions deviating from the expansion through the gravitational interactions with the surrounding matter. The resulting velocity is called the peculiar velocity. The peculiar velocity of galaxies directly traces the evolution of the large-scale structures and matter flows in the cosmic web. At the present day, the filamentary network contains almost half of the matter in the universe. This makes filaments perfect laboratories for studying the galaxy flows. The filaments are believed to act as cosmic highways, transporting matter into clusters of galaxies.

With constantly improving theoretical and technological methods, observations of the cosmic web can reach both into larger scales and more detailed description of its constituents. At the same time, with continuously improving computational power, numerical simulations are able to model the universe at cosmologically relevant scales. Hydrodynamical simulations, such as the EAGLE, can be used to explain and predict observational results of galaxy evolution in the context of the cosmic web. Such simulations offer an unique way to study galaxy flows in the three dimensions, which would not be otherwise possible.

In this thesis, using the state-of-the-art EAGLE simulation, the peculiar motions of galaxies are studied inside and around of filaments. For this purpose, the

filament catalog made by Ganeshaiah Veena et al. (2019) using the Bisous method is utilised. The aim is to find out how the filament environment affects the galaxy flows. This is done by comparing peculiar motions inside and outside of filaments and by studying the peculiar motions with the geometrical properties of filaments and the baryonic properties of galaxies reflecting the galaxy evolution. These are measured with fixed group mass to avoid the effect of the local environment on the peculiar motions. This thesis is organised as follows. In Chapter 1 the cosmological background of structure formation is described, while Chapter 2 introduces the basics of cosmological simulations and the EAGLE simulations. Chapter 3 focuses on the cosmic web and briefly describes different filament finding methods, including the Bisous method. In Chapter 4 the data is introduced and analysed, while in Chapter 5 the main results are summarised.

1 Cosmological background

Cosmology is the study of our universe as a whole, how it came to be and how it evolves, as well as how the structures we observe form in this cosmological framework. The starting point of the cosmic evolution is considered to be a very dense and hot initial state, the big bang, after which the universe has been continuously expanding and cooling. During the early phases, the universe undergoes a cosmic inflation, a phase when the universe expands exponentially and fluctuations are generated that seed the present day structure, the cosmic web of filaments and clusters of galaxies separated by empty voids. The theory of the big bang and cosmic inflation are part of the current standard model of cosmology, the ΛCDM model, where Λ is the cosmological constant associated with dark energy and CDM stands for the cold dark matter. This model is based upon the cosmological principle, the assumption of the universe being spatially homogeneous and isotropic. The second cornerstone of this paradigm is that gravity is the dominating force on scales relative to cosmology and is accurately described by the general theory of relativity. The complete mathematical framework for the cosmological background introduced in this chapter can be found in textbooks by Schneider (2006) and Mo et al. (2010).

1.1 Expanding universe

In the general theory of relativity formulated by Einstein in 1915, the geometry of space-time is determined by the matter and energy distribution in the universe. This relation is expressed through the Einstein field equations

$$R_{\mu\nu} - \frac{1}{2} g_{\mu\nu} R + g_{\mu\nu}\Lambda = \frac{8\pi G}{c^4} T_{\mu\nu}, \tag{1}$$

where $R_{\mu\nu}$ is the Ricci curvature tensor, $g_{\mu\nu}$ is the metric tensor, R is the scalar curvature, G is the Newton's gravitational constant, c is the speed of light and $T_{\mu\nu}$ is the energy–momentum tensor describing the matter and energy content of

the Universe. The cosmological constant Λ was originally introduced to oppose the gravitational attraction and allow solutions for static world models, but was set aside following Hubble's discovery in 1928 of the expanding universe. It was not until the confirmation of the accelerated expansion of the universe (Riess et al. 1998; Perlmutter et al. 1999) that the cosmological constant was considered as a key component modelling our universe, corresponding to the dark energy not only balancing the gravitational attraction, but driving the expansion.

The left-hand side of the field equations represents the curvature of space-time determined by the metric. For homogeneous and isotropic universe it can be given by the Robertson–Walker metric. In spherical coordinates the space-time distance between two points is

$$ds^2 = -c^2dt^2 + a^2(t)\left[\frac{dr^2}{1-kr^2} + r^2(d\theta^2 + \sin\theta^2 d\phi^2)\right]. \tag{2}$$

Here (r, θ, ϕ) are comoving coordinates and the constant k represents the curvature of space and can take a value -1, 0 or 1, corresponding to an open, flat or closed universe. The scale factor $a(t)$ describes the expansion of the universe and with it the expansion rate, the Hubble parameter, is defined

$$H(t) \equiv \frac{\dot{a}(t)}{a(t)}. \tag{3}$$

If the matter and energy content of the universe is described as an uniform ideal fluid, the field equations solved together with Robertson–Walker metric gives the following equations;

$$\frac{\ddot{a}}{a} = -\frac{4\pi G}{3}\left(\rho + 3\frac{P}{c^2}\right) + \frac{\Lambda c^2}{3}, \tag{4}$$

$$\frac{\ddot{a}}{a} + 2\left(\frac{\dot{a}}{a}\right)^2 + 2\frac{kc^2}{a^2} = 4\pi G\left(\rho - \frac{P}{c^2}\right) + \Lambda c^2. \tag{5}$$

Combining these two yields

$$\left(\frac{\dot{a}}{a}\right)^2 = \frac{8\pi G}{3}\rho - \frac{kc^2}{a^2} + \frac{\Lambda c^2}{3}. \tag{6}$$

Equations (4) and (6) are considered as the Friedmann equations, where ρ is the total density of the universe and P is the total pressure. They represent world models known as the Friedmann–Robertson–Walker (FRW) cosmological models. In the case where cosmological constant is neglected and $k = 0$, the solution of equation (6) becomes as

$$\rho_{\mathbf{crit}} = \frac{3H^2}{8\pi G}. \tag{7}$$

This critical density is used to define the dimensionless total density parameter

$$\Omega \equiv \frac{\rho}{\rho_{\mathbf{crit}}}. \tag{8}$$

The total density parameter is the sum of density parameters for each matter-energy component of the universe; baryonic matter $\Omega_{\rm b}$, dark matter $\Omega_{\rm DM}$, dark energy Ω_Λ and radiation $\Omega_{\rm r}$. These are conventionally used to characterise cosmological models. In the present day, most important constituents are the dark energy, dark matter and baryonic matter.

1.2 Peculiar velocity

The expansion of the universe was confirmed by the observation of galaxies moving away from us, receding faster the further away they were, resulting in a linear relation between galaxy's radial velocity and the galaxy's distance from the observer,

$$v_{\rm r} \propto H_0 r, \tag{9}$$

where the Hubble constant H_0 is the current value of the expansion rate of the universe, usually expressed in a dimensionless form, $h \equiv H_0/100\ \mathrm{kms^{-1}Mpc^{-1}}$. But not only the cosmic expansion decide a galaxy's motion. The total velocity is the sum of several velocity components originating from different sources on small and large scales. The Andromeda galaxy is approaching the Milky way at the speed of ~ 110 km/s with respect to the Milky Way's rest frame (van der Marel et al. 2012).

Galaxies in groups are affected by the group's gravitational potential and can have velocity dispersions of 1000 km/s in rich clusters (Struble & Rood 1999). Our Local group is moving 631 km/s towards the Great attractor relative to the cosmic microwave background (Fixsen et al. 1996). These velocities are collectively known as the peculiar velocity $v_{\rm pec}$, which is the deviation from the expansion velocity, the Hubble flow. Thus, in the precise form the equation (9) is

$$v_{\rm tot,r} = v_{\rm pec,r} + H_0 r, \tag{10}$$

which can be generalised further to give the three-dimensional peculiar velocity vector at time t,

$$\mathbf{v}_{\rm pec} = \mathbf{v}_{\rm tot} - H(t)\mathbf{r}, \tag{11}$$

where $H(t)$ is the Hubble parameter defined in equation (3).

To obtain galaxy peculiar velocities from observations, the total radial velocity must be known as well the distance to the object. Radial velocities can be measured through the Doppler shift of spectral lines, while for redshift independent distance measurements there exists several methods, called the cosmic distance ladders. Most of them are based on luminosity measurements as the distance depends on the apparent magnitude m and on the absolute magnitude M through

$$r = 10^{1+(m-M)/5}. \tag{12}$$

With growing distance, the uncertainties in measurements also grow. The amplitude of uncertainties in peculiar velocities can become larger than the actual peculiar velocity of the galaxy. Thus, in deep galaxy surveys the only way to determine distances is with redshift measurements. Peculiar velocities can cause different redshift-space distortions. This is because observations in general can only provide information on the line-of-sight component of the velocity. Galaxies in and near groups and clusters appear as elongated structures pointing towards the observer in the redshift space due to high velocities towards and away of the observer. This

effect is known as the "Finger of God" effect. In larger scales, coherent galaxy flows towards massive structure can cause an apparent flattening of the structure, which is called the Kaiser effect. The only way to study 3D peculiar velocities of individual galaxies in cosmological scales is with numerical simulations. Studying the 3D galaxy velocities in simulations can help to understand effects seen in the observations of galaxy flows.

The peculiar velocities originate from local gravitational fields that give rise to acceleration and motion deviating from the pure Hubble flow. These gravitational fields are generated by the non-uniform matter distribution in the universe.

1.3 Structure growth

Despite the cosmological principle of the universe being homogeneous and isotropic, there must be inhomogeneities proven by our very existence and ability to observe complex structures. However, the universe can be considered as homogeneous on large scales, as seen in Figure 1. The small scale inhomogeneities must already be present on very early times as they are imprinted on the cosmic microwave background (CMB) as small temperature fluctuations, radiation originating from the epoch of recombination $\sim$ 380 000 years after the big bang. These small fluctuations originate from the cosmic inflation, an extension to the standard model where the universe expands very rapidly after the big bang. During this inflationary phase quantum fluctuations are amplified to larger scales becoming the seeds of the observed structures. These density perturbations are characterised by the density contrast

$$\delta(\mathbf{x}, t) \equiv \frac{\rho(\mathbf{x}, t) - \bar{\rho}(t)}{\bar{\rho}(t)}, \tag{13}$$

which relates the matter density $\rho(\mathbf{x})$ at the position $\mathbf{x}$ at time t to the mean matter density of the universe $\bar{\rho}(t)$ at that moment. Statistical examination of the density

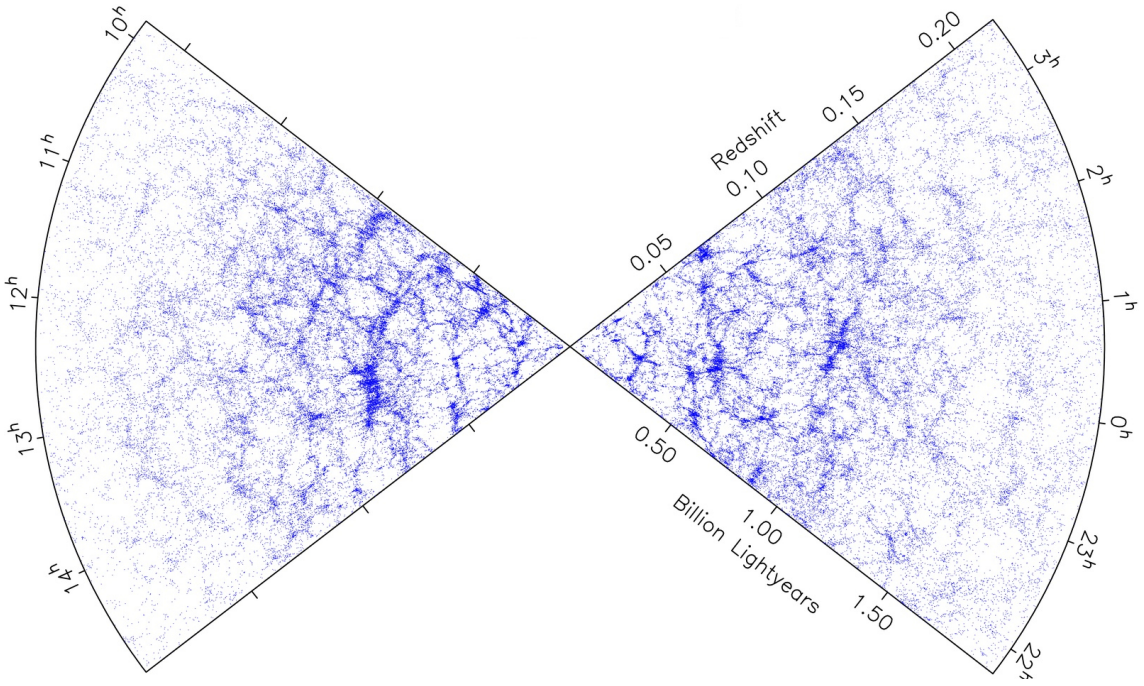

Figure 1: The spatial distribution of galaxies in the 2dF Galaxy Redshift Survey projected onto the redshift–right ascension plane (Colless et al. 2003).

field is enabled through the power spectrum

$$P(k,t) = \langle |\delta(k,t)|^2 \rangle. \tag{14}$$

Here $\delta(k,t)$ is the Fourier transform of the density field $\delta(\mathbf{x},t)$, consisting of components with comoving wavenumber k. The inflationary phase naturally produces an initial density field that is a homogeneous and isotropic Gaussian random field. This makes the power spectrum an effective tool describing the density perturbations as the statistical properties of such a field can be completely specified by it.

The density perturbations grow through self-gravity in an expanding background. Overdense regions with density contrast $\delta > 0$ expand more slowly than the Hubble expansion, while regions with $\delta < 0$ expand faster. Hence, through this gravitational instability, overdense regions are amplified over time, eventually leading to the formation of large-scale structures. The evolution of density perturbations can be examined in two distinct phases; the linear phase when perturbations are small,

$|\delta| \ll 1$, and in the non-linear phase $|\delta| \gg 1$, when overdense regions detach from the expansion and start to collapse and form structures.

1.3.1 Linear regime

In the linear perturbation theory, the density of the universe is taken to mainly consist of matter, which can be described as a non-relativistic ideal fluid under Newtonian gravity as long as the mean free path of particles is much smaller than the spatial scale of the density perturbations. The evolution of an ideal fluid can be followed by the continuity equation describing the mass conservation, the Euler equation giving the equations of motion and the Poisson equation for the gravitational potential. For a fluid element moving with velocity $v_{\rm pec}$ in a an expanding background these equations are written as

$$\frac{\partial \delta}{\partial t} + \frac{1}{a}\nabla \cdot [(1+\delta)\mathbf{v}_{\rm pec}] = 0 \tag{15}$$

$$\frac{\partial \mathbf{v}_{\rm pec}}{\partial t} + \frac{1}{a}(\mathbf{v}_{\rm pec} \cdot \nabla)\mathbf{v}_{\rm pec} + \frac{\dot{a}}{a}\mathbf{v}_{\rm pec} = -\frac{\nabla P}{a\bar{\rho}} - \frac{\nabla \phi}{a} \tag{16}$$

$$\nabla^2 \phi = 4\pi G a^2 \bar{\rho}\delta. \tag{17}$$

If only small density perturbations are considered, the above equations can be linearised, and if the fluid is taken to consist of pressureless matter, a second-order differential equation for the density contrast can be obtained:

$$\frac{\partial^2 \delta}{\partial t^2} + 2\frac{\dot{a}}{a}\frac{\partial \delta}{\partial t} = 4\pi G\bar{\rho}\delta. \tag{18}$$

This equation has two linearly independent solutions, a growing and a decaying mode. Here the interest is focused on the growing solution for the density contrast

$$\delta(\mathbf{x}, t) = \delta_i(\mathbf{x})D(t), \tag{19}$$

where $\delta_i(\mathbf{x})$ is the density contrast at some initial time t_i, and the growth factor $D(t)$ describes the growth in the amplitude of the density perturbations. The growth factor depends on the density of the universe and has the form

$$D(a) \propto \frac{H(a)}{H_0} \int_0^a \frac{da'}{[\Omega_\mathrm{m}/a' + \Omega_\Lambda a'^2 - (\Omega_\mathrm{m} + \Omega_\Lambda - 1)]^{3/2}}, \tag{20}$$

if the total density is taken to consist of dark energy and matter, $\Omega_\mathrm{m} = \Omega_\mathrm{b} + \Omega_\mathrm{DM}$.

To follow the growth of the density perturbations, it is more convenient to use a statistical approach as the complete functional form of the density field can not be realised in a particular universe. In the statistical sense, the growth of density perturbations can be followed through the evolution of the power spectrum $P(k)$. The equations (14) and (19) imply that in the linear theory the equivalent power spectrum is

$$P(k,t) = P_i(k) D(t)^2. \tag{21}$$

The initial power spectrum $P_i(k)$ of density perturbations is commonly assumed to be a power law, $P(k) \propto k^n$. In the early universe the amplitude of density perturbations is expected to be equal on all scales, resulting in a scale-invariant form for the initial power spectrum with spectral index $n = 1$, also known as the Harrison–Zel'dovich spectrum.

In the linear perturbation theory the universe is assumed to be matter-dominated, while neglecting relativistic effects and assuming the matter to be a pressureless fluid. However, the evolution of density perturbations depends on the matter-energy content of the universe through the growth factor. In addition, in the early radiation-dominated era the evolution depends on the scale of the density perturbations. Due to this a correction term, a transfer function $T(k)$, is introduced to connect the initial conditions to the post-recombination power spectrum

$$P(k,t) = P_i(k) D(t)^2 T^2(k). \tag{22}$$

Although the shape of the linear power spectrum can be determined from theory, the

amplitude must be measured from observations. The power spectrum is normalised with the variance $\sigma(R)$ of the galaxy distribution when sampled with randomly placed spheres of radii R. In the local universe the variance is about unity for $R = 8h^{-1}$Mpc, thus the amplitude is usually represented by the value σ_8.

Local density perturbations generate local gravitational fields which lead to acceleration in particle motions. This acceleration gives rise to peculiar velocities. As the perturbations in velocities and densities are intertwined together, the linear evolution of the velocity field can be determined from the linear theory for the evolution of the density field. Combining the solution for density field with the continuity equation gives the divergence of the velocity field,

$$\nabla \cdot \mathbf{v}_{\rm pec} = -aH(t) f(\Omega_{\rm m}, \Omega_\Lambda)\delta, \tag{23}$$

where the function

$$f(\Omega_{\rm m}, \Omega_\Lambda) \equiv \frac{a}{D}\frac{dD}{da} \tag{24}$$

is the linear growth rate. Its dependence on the cosmological constant is negligible and at $t = t_0$ can be approximated with $f(\Omega_{\rm m}) \approx \Omega_{\rm m}^{0.6}$ (Peebles 1980).

The equation (23) shows that the peculiar velocity and density fields are completely determined by each other. In the linear regime peculiar velocity flows offer a way to follow the underlying matter distribution as it not only traces the luminous galaxies but the whole gravitating mass inducing the velocities. The total density field can be represented by galaxy distribution with some bias. If this bias is known, the comparison between predicted and measured velocity field would give an estimate for the linear growth rate and the matter density parameter.

As in the case of density field, the statistical properties of the velocity field can be described with power spectrum. The velocity power spectrum is proportional to the matter power spectrum by

$$P_v(k) = a^2 H(t)^2 f(\Omega_{\rm m}, \Omega_\Lambda)^2 P(k) k^{-2}. \tag{25}$$

With a given matter power spectrum, the present day variance of the linear velocity field can be determined,

$$\sigma_v^2 = \frac{H_0^2 f(\Omega_\mathrm{m})^2}{2\pi^2} \int_0^\infty P(k) dk. \tag{26}$$

The variance corresponds to the linear contribution from velocity fluctuations on scales larger than the sampled region. With simulation data, it gives the linear velocity induced by scales larger than the simulation box size L (Suhhonenko & Gramann 2003),

$$v_L^2 = \frac{H_0^2 f(\Omega_\mathrm{m})^2}{2\pi^2} \int_0^{2\pi/L} P(k) dk. \tag{27}$$

1.3.2 Non-linear regime

The linear perturbation theory for structure growth becomes unsuitable when a density contrast grows beyond the linear limit, $\delta \sim 1$. Only some special cases exist when the growth has a analytical solution. The spherical collapse model is the basis of the successful model for estimating the number density of dark matter halos as a function of their mass and redshift by Press & Schechter (1974). In the spherical collapse model, overdensities are enclosed by a sphere of radius R and the matter distribution is considered to be homogeneous inside the sphere. In this approach a density perturbation is assumed to be an isolated FRW-model universe with a density larger than the critical density ρ_crit. In the course of time the perturbation expands until a turnover point, when it begins to collapse under its own gravity. The growth is decelerating before the turnover, a point when R has its maximum size. During the turnover, the evolution of the density perturbation becomes nonlinear as it detaches from the expansion of the space and starts to collapse. The perturbation shrinks, collapses and virialises.

For a matter dominated universe where $\Omega_\Lambda = 0$, the density of a virialised structure is $\rho_\mathrm{vir} = (1 + \delta(t_\mathrm{vir}))\bar{\rho}_\mathrm{vir} \approx 178\bar{\rho}_\mathrm{vir}$, a result from the conservation of energy and the virial theorem. From this follows that a virialised region has an average

density of ~ 200 times the critical density of the universe at the time of the collapse. This is the basis for the typically used definition for a dark matter halo, a virialised matter concentration that has the density of $200\rho_{\rm crit}$ within a sphere with radius R_{200} that encloses the halo mass M_{200}.

In a strict sense, a density perturbation collapses into a singularity in the spherical collapse model if the matter distribution is homogeneous. Actual overdensities have density fluctuations within them, making the collapse occur at different time in different regions. For halos with density profile decreasing outwards, the collapse of inner shells occurs before of outer ones in the process also known as violent relaxation.

Although the spherical collapse model can describe the nonlinear evolution of galaxy dark matter halos, for a generic triaxial perturbations the collapse is expected to result as a flattened quasi two-dimensional structures, often called as "pancakes" (Lin et al. 1965). Gravitational collapse amplifies any anisotropies present in the initial density field giving rise to asymmetrical structures, as seen in Figure 1. This anisotropic collapse of matter can be described by the Zel'dovich approximation (Zel'dovich 1970).

The Zel'dovich formalism describes the formation and evolution of the cosmic structure with first order Lagrangian approximation for the motion of a collisionless fluid element, relating the initial Lagrangian coordinates $\mathbf{q}$ and comoving Eulerian coordinates $\mathbf{x}$. Assuming irrotational motion and restricting the solution to the growing mode leads to a ballistic displacement of the Eulerian position at time t,

$$\mathbf{x}(t) = \mathbf{q} + D(t)\mathbf{\Psi}(\mathbf{q}), \tag{28}$$

where $D(t)$ is the linear growth factor and $\mathbf{\Psi}(\mathbf{q})$ is the initial displacement field. The evolution of the density field is given by

$$\rho(\mathbf{x}, t) = \frac{\bar{\rho}}{[1 - D(t)\lambda_1(\mathbf{q})][1 - D(t)\lambda_2(\mathbf{q})][1 - D(t)\lambda_3(\mathbf{q})]}, \tag{29}$$

where $\lambda_1 \geq \lambda_2 \geq \lambda_3$ are the three eigenvalues of the deformation tensor,

$$\mathbf{\Psi}_{ij}(\mathbf{q}) = \frac{\partial^2 \Psi(\mathbf{q})}{\partial q_i \partial q_j}. \tag{30}$$

The absolute values of these eigenvalues give the lengths of the three axes of the deformation ellipsoid. Positive value corresponds to compression and negative value expansion along the axis. Two-dimensional sheets, the pancake structures, emerge from the collapse of the axis corresponding to the largest eigenvalue λ_1. Filamentary structure emerges when the collapse occurs along the two longest axes. Clusters arise from the collapse along all three axes while voids are defined by the expansion along these axes.

The approximation breaks down after the formation of pancakes, when there is shell crossing. Particles will oscillate in the gravitational potential and do not follow the predicted trajectories. Following the formalism, the particles would stream away. The adhesion model adds a viscosity term to ensure that the particles stick together at shell crossing and form structures (Shandarin & Zel'dovich 1989). Due to its simplistic yet accurate nature of describing structure formation in the linear and mildly non-linear stages, the Zel'dovich formalism is a powerful tool for setting the initial positions and velocities in cosmological simulations.

1.4 The ΛCDM model

The currently favoured model for the standard cosmological model is the ΛCDM model, in which the universe is considered to be flat and the total density consist of $\sim 70\%$ of dark energy, $\sim 25\%$ of cold dark matter and $\sim 5\%$ of baryonic matter. The ratio of the components making up the total density has evolved through the cosmic history. In the very early universe before the matter dominating era, relativistic particles made up the bulk of the total density and baryonic matter was in in the form of hot plasma. After the epoch of recombination, when the universe had cooled down such that atoms could have formed, photons decoupled from the

Table I: Cosmological parameters from the Planck Collaboration (2013). From left to right the parameters are the density parameters of dark energy, dark matter and baryonic matter at $z \sim 0$, the dimensionless Hubble parameter, the linear variance of the matter distribution smoothed with a top-hat filter of radius 8 h^{-1} Mpc, the spectral index of the power spectrum of initial adiabatic perturbations.

Ω_Λ	$\Omega_{\rm DM}$	$\Omega_{\rm b}$	h	σ_8	n
0.693	0.259	0.048	0.678	0.829	0.961

baryonic matter making the universe transparent. The photons originating from this era are now observed as the 2.73 K cosmic microwave background radiation. Cosmological parameters derived for the ΛCDM model from the measurements of the CMB anisotropies and used in the EAGLE simulations are listed in Table I.

In the present day the universe is dominated by dark energy, responsible for the expansion of space with accelerating speed. The nature of dark energy remains as a mystery in the standard cosmology. The same is for the dark matter, which constitutes most of the matter density and interacts only through gravity. It is assumed to be cold, meaning that the particle velocities are non-relativistic. Currently favoured candidate for the cold dark matter is the hypothetical WIMP, weakly interacting massive particle. Yet any candidate particle eludes detection.

The initial density perturbations of cold dark matter have larger amplitudes on smaller scales, making the smaller overdensities collapse first. The collapsed dark matter concentrations, dark matter halos, grow from the merging of smaller mass halos into larger ones. This hierarchical scenario can be seen in the presence of galaxies already at early times, whereas clusters of galaxies become abundant only at $z \lesssim 1$. The formation of galaxies and the large-scale structure in the ΛCDM-model and in other cosmological models can be studied by cosmological simulations with the aim to predict and explain observational results.

2 Cosmological simulations

The cosmic evolution of hierarchical structure formation from small density fluctuations to the present day large-scale structures is a tangled chain of events with various physical processes. The amount of particles involved in these interactions inhibits any analytical solutions, and due to this cosmological simulations are developed to model structure formation in the expanding universe with numerical methods. The same subjects that are considered in this chapter are also thoroughly covered in the review article by Vogelsberger et al. (2020).

Creating a virtual universe comes with limitations. Unlike the infinite space, simulations are restricted by a finite volume. To mimic an infinite volume, simulations have periodic boundary conditions, meaning that a particle leaving the simulation box will re-enter from the opposing side. For the simulation to be cosmologically meaningful, the box size L has to be larger than the observed large-scale structures. The simulation volume is a compromise between the simulation mass resolution as the contained total mass is $\Omega_{\mathrm{m}}\rho_{\mathrm{crit}}L^3$, so for a given number of particles the mass resolution is set. These simulation particles are defined as mass elements representing multiple particles, as it is impossible to simulate the amount of real particles governing galaxy formation due to computing resources.

A cosmological simulation starts with the definition of initial conditions. Initial conditions are created by first generating an uniform and unperturbed particle distribution and then imposing density perturbations. An uniform distribution can be made by distributing the simulation particles into a regular cubic grid or a glass-like configuration (Baugh 1995). The next step is to realise a linear density field, which is in the concordance model of cosmology a Gaussian random field with its characteristics completely described by the power spectrum $P(k)$. Then initial positions and velocities are assigned by displacing particles using the Zel'dovich approximation or low-order perturbation theory (e.g. Jenkins 2010). The initial baryon temperature

is often chosen to be the equivalent to the microwave background temperature at the initial redshift of the simulation.

Starting from the initial conditions the motion of particles is integrated forward in time with small time-steps. The dark matter particles interacting only through gravity can be described as a collisionless fluid with motion defined by the collisionless Boltzmann equation coupled to the Poisson equation. Solving the gravitational force for each particle by direct summation is not efficient and instead N-body methods are used. Most of the gravity algorithms can be divided into two categories; the particle-based methods approximating the direct summation and the mesh-based methods.

The most commonly used particle-based method is the tree algorithm (Barnes & Hut 1986), a hierarchical multipole expansion. The algorithm groups up particles based on the distance to the particle for which the forces are calculated. Instead of calculating the forces between each particle, the force is measured between the particle and the center of mass of the grouped up particles. The particle-mesh algorithm, i.e. the PM-method (Hockney & Eastwood 1981), divides the simulation volume into a grid of meshes. In this method particle masses are distributed to grid points and the corresponding force field is obtained from the gravitational potential calculated with fast Fourier transform. Forces affecting a particle are obtained by interpolating them back to the particle position. Within this method the simulation resolution can be increased by implementing a set of nested grids, leading to a category of adaptive mesh refinement schemes. In order for the particle distribution to correctly represent a collisionless fluid, unwanted two-body scatterings are avoided by introducing a softening length ϵ to soften the gravitational force between particles. This defines the force resolution of the simulation and dictates the spatial scale of smallest detectable objects. In the mesh-based algorithms no additional softening is needed as the force is automatically smoothed on the mesh-scale.

2.1 Hydrodynamical simulations

Simulating the dark component of matter is rather straightforward compared to the ordinary, baryonic matter, due to the broad range of physical processes involved in galaxy formation. Still, it is fundamental as it constitutes all of the visible Universe. In hydrodynamical simulations baryonic particles and processes are modelled in addition to the dark matter particles that provide the bulk of the gravitating mass. These simulations treat the baryonic matter as an inviscid ideal fluid of which motion is determined with a set of hydrodynamical equations, consisting of the continuity equation, the Euler equation and the first law of thermodynamics. The different methods created to solve the fluid motion can be divided into two categories, depending on how the equations are discretised; the Lagrangian and the Eulerian methods

In the Eulerian methods the simulation space is discretised by volume elements through which the fluid flows. The Eulerian methods are the more traditional approach, with various schemes created to solve the hydrodynamical equations. The adaptive-mesh-refinement schemes enable the adjusting of mesh sizes to obtain a higher resolution in a high density region. Unlike the Eulerian methods, the Lagrangian methods discretise the fluid by mass elements which move through space. Most of the Lagrangian methods are variants of the smoothed particle hydrodynamics method, i.e. SPH, first developed by Lucy (1977) and Gingold & Monaghan (1977). In the SPH particles interact with each other through a symmetric kernel function with a radius called the smoothing length. Inherently the SPH has adaptive spatial resolution as the mean particle distances are smaller in higher density regions.

Because of the limited resolution in simulations and the complex nature of physical processes of galaxy formation, most of these processes cannot be modelled from first principles but need to be implemented on the sub-resolution scale with effective

models. Physical models that hydrodynamical simulations often consider are e.g. cooling of the baryonic gas, interstellar medium, star formation, supermassive black holes and the stellar and active galactic nuclei feedback. These sub-resolution models depend on a number of parameters that are often calibrated through observations.

From these baryonic processes only gas cooling is not implemented as sub-resolution model but through pre-computed tabulated cooling function included in the first law of thermodynamics. The important cooling processes include bremsstrahlung emission, recombination, collisional excitation and ionisation, inverse Compton and the cooling due to metals and molecules. The interstellar medium (ISM) is often modelled to have a multi-phase structure, where the cold star forming regions are embedded in a hot medium. The cold gas can be transformed into collisionless star particles. The stellar populations are characterised by an initial stellar mass function. The converting of gas into stars is based on star formation rate and often done using probabilistic sampling schemes. Commonly some criteria for gas elements is set limiting the number eligible for star formation. Simulations also often track the mass loss from stellar components to account for the metal enrichment of the ISM.

Without a source that can heat the star forming interstellar medium, the gas can overly condensate leading to the cooling catastrophe. Various feedback processes counteract this by the injection of energy and momentum leading to a loop regulating the star formation. These feedback processes need to be powerful enough to eject gas out of galaxies, creating galactic winds. Supernovae introduce the most efficient form of stellar feedback generating these winds, other significant channels being stellar winds, photoionisation and radiation pressure from young massive stars. The sub-resolution models of the stellar feedback most differ in the way that the energy is deposited to the gas, either thermally or kinetically. In more massive halos active galactic nuclei (AGN) becomes the dominant feedback source with relativistic

jets and non-relativistic outflows. The AGN feedback is commonly divided in two modes that are implemented differently, quasar and radio mode. The quasar mode is associated with the radiatively efficient mode of growth of a supermassive black hole (SMBH), running as the engine of the AGN. The radio mode associated with the relativistic jets is implemented once the accretion rate of the SMBH is below a critical value. Simulations have to numerically seed the black holes in dark matter halos as they cannot be otherwise resolved.

In addition to the intertwined star formation and feedback processes within the interstellar medium, other physical processes have been considered in hydrodynamical simulations. Such are e.g. cosmic rays, which provide an additional feedback channel, and magnetic fields shaping the ISM. These are not however in the scope of this thesis as they are also not considered in the EAGLE simulations.

2.2 The EAGLE simulations

The Virgo Consortium's EAGLE (Evolution and Assembly of GaLaxies and their Environments) project is a suite of cosmological hydrodynamical simulations aimed to better understand the formation and evolution of galaxies and is described in Schaye et al. (2015) by the following way. The simulations use the standard ΛCDM cosmology with cosmological parameters from the Planck Collaboration 2013 results. They are run with a modified version of the GADGET-3 code, which follows a collisionless fluid with N-body method and employs smoothed particle hydrodynamics for ideal gas (Springel 2005). The gravitational forces are computed with a hybrid TreePM algorithm, where the short-range forces are computed with the particle-based tree-method and long-range forces with the mesh-based PM-method. This thesis utilised the largest-volume simulation run with comoving box size $L =$ 100 Mpc. Simulation parameters for this run are specified in Table II.

The initial conditions were created by producing a particle load with a Gaussian

Table II: The largest-volume Eagle simulation parameters. From left to right the columns show the simulation identifier, comoving box size, total number of particles, initial baryonic particle mass, dark matter particle mass and the maximum proper softening length.

Identifier	L [Mpc]	N	$m_{\rm b}$ [$\rm M_\odot$]	$m_{\rm DM}$ [$\rm M_\odot$]	$\epsilon_{\rm phys}$ [kpc]
Ref-L0100N1504	100	2×1504^3	1.81×10^6	9.70×10^6	0.70

random density field. The linear matter power spectrum was generated from a power-law primordial power spectrum and from a dark matter transfer function evaluated at present day. Particle displacements and velocities were calculated from initial glass-like configuration with second order Lagrangian perturbation theory.

The main modifications made on the GADGET-3 code and applied in the EAGLE simulations consider the formulation of SPH, the time stepping and the sub-resolution physics. Sub-resolution models are crafted for star formation, stellar mass loss and metal enrichment, radiative cooling, gas accretion onto and mergers of supermassive black holes, energy feedback from star formation and AGN feedback. Apart from stellar mass loss, all of the effects of stellar processes are captured with only one type of stellar feedback. The feedback from AGN is also employed through only one mode. The feedback energy is injected thermally and the efficiency of the stellar feedback is calibrated to match the observed present day galaxy stellar mass function, also taking galaxy sizes into account, while the efficiency of the AGN feedback is calibrated to the observed relation between stellar and black hole mass.

The galaxies in the EAGLE simulations are defined as gravitationally bound subhalos identified by the SUBFIND algorithm (Springel et al. 2001; Dolag et al. 2009), which finds dark matter halos with the Friends-of-Friends algorithm (Davis et al. 1985). This algorithm defines halos based on the spherical collapse model as structures where particles are separated by distances less than the linking length, by convention chosen to be 0.2 times the mean interparticle separation. The gas

and star particles are assigned to the same dark matter halo as their nearest dark matter particles. The substructures within the dark matter halo are defined as overdense regions, consisting of any type of particles, bounded by saddle points in the density distribution. The subhalos are obtained by removing the particles that are not gravitationally bound to the substructures. To remove non-physical low-mass subhalos dominated by a single massive particle such as a supermassive black hole, subhalos separated by less than 3 kpc and the stellar half-mass radius are merged. In the dark matter halo the central galaxy is defined as the subhalo containing the particle with the gravitational potential minimum while other subhalos are assigned as satellite galaxies. Figure 2 shows a slice through the largest-volume run at $z = 0$, color-coded by the gas temperature, which zooms in on an individual galaxy, showing the stellar light after accounting for dust extinction.

The EAGLE simulations are found to be in agreement with observations of low-redshift galaxy specific star formation rates, passive galaxy fractions, Tully–Fisher relation and column density distributions of intergalactic metals. In the Ref-L0100N1504 simulation the stellar mass-metallicity relations for the interstellar medium and stars are less steep than extrapolations of observations for $M_* \lesssim 10^{10}$ $M_\odot$. In galaxy clusters the gas fractions and luminosities are found to be too high compared to X-ray observations of the intra-cluster medium. A better agreement between the mass-metallicity relations and observations can be achieved by increasing the efficiency of the feedback from star formation. In the low-mass tail of galaxy clusters the gas fractions and X-ray luminosities can be fixed by increasing the heating temperature of the AGN feedback. Re-runs with these modified feedback models do not include $L = 100$ Mpc simulations.

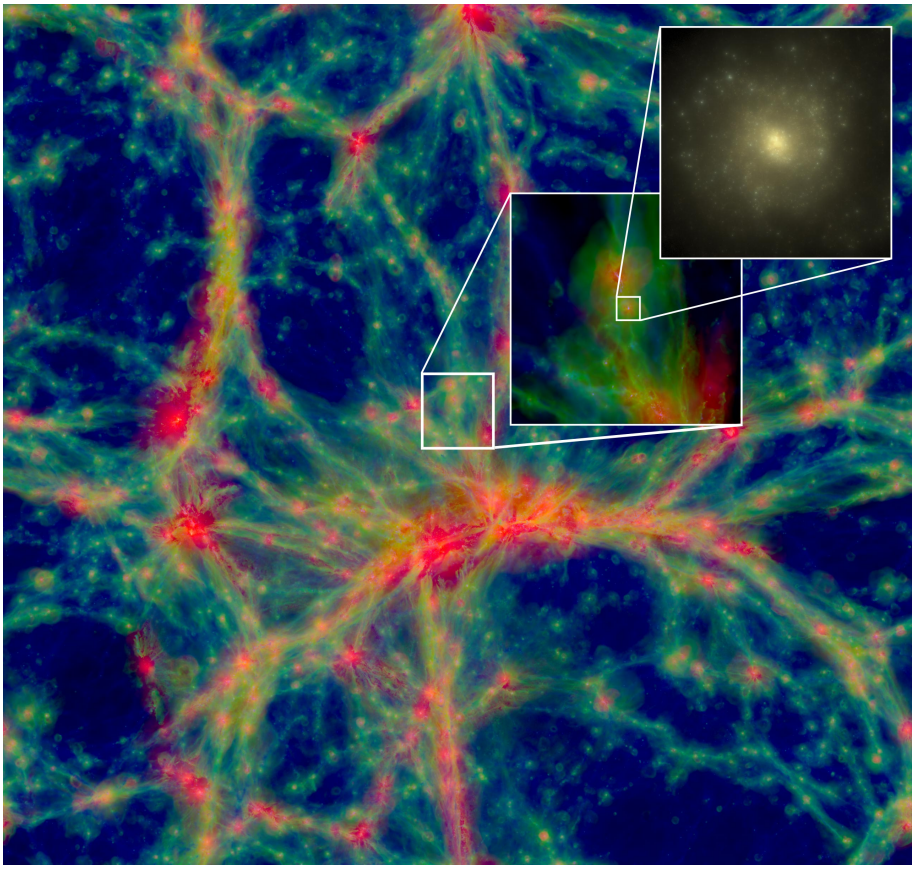

Figure 2: A $100 \times 100 \times 20$ Mpc slice through the Ref-L0100N1504 simulation at $z = 0$. The red color shows gas with $T > 10^{5.5}$ K, green $10^{4.5} < T < 10^{5.5}$ K and blue $T < 10^{4.5}$ K. In the first zoom-in $L = 10$ Mpc. In the second zoom-in $L = 60$ kpc and the stellar light is based on monochromatic u, g and r band SDSS filter means and accounting for dust extinction (Schaye et al. 2015).

3 The cosmic web

The galaxies in the universe are not randomly distributed, but are clustered together on scales of a few up to more than a hundred megaparsec (van de Weygaert & Schaap 2009) forming a foam like pattern, known as the cosmic web (Jõeveer & Einasto 1978; Bond et al. 1996). Originating from the anisotropic gravitational collapse and as the result of hierarchical evolution, the cosmic web is multiscale in its nature and fills the whole observable universe.

3.1 Components of the cosmic web

The cosmic web is built up of dense knots, elongated filaments, two-dimensional walls and near-empty voids, features that can be seen in Figures 1 & 2. The knots are the intersections of the cosmic web where clusters up to thousands of galaxies concentrate. Galaxy clusters are the most massive and recently gravitationally collapsed objects. They can be observed by X-ray emission emerging from the hot and diffuse gas inhabiting the intra-cluster medium. On larger scales, structures are assembled into superclusters, giant agglomerations of hundreds of thousands of galaxies. The Milky way is a part of the Laniakea supercluster (Tully et al. 2014), stretched out to 160 Mpc and encompasses 10^{17} solar masses. At the core of the Laniakea is the Great attractor (Lynden-Bell et al. 1988).

The walls are tenuous, sheet-like structures. They are visually much less prominent than the other cosmic web components, except for voids, as the galaxies within walls are less numerous and less luminous (Cautun et al. 2014). On larger scales clusters can be found in flattened supercluster configurations, known as great walls. The largest known wall structure is the BOSS great wall, with the volume of $2.4\times10^5 h^{-1}$ Mpc^3 (Lietzen et al. 2016). Other outstanding wall structures are the Sloan great wall (Gott et al. 2005) and the South pole wall (Pomarède et al. 2020).

Voids are enormous regions nearly empty of galaxies enclosed by filaments, clusters and walls. Usually roundish in shape and sizes of 20–50 h^{-1} Mpc they occupy $\sim 80\%$ of the space in the universe but contain only $\sim 20\%$ of the total mass (Platen et al. 2007; Cautun et al. 2014). In the immediate vicinity of our home galaxy is the Local void that has a diameter of 30 Mpc (Tully & Fisher 1987). The void regions offer one of the cleanest probes of dark energy and tests of gravity and general relativity as their structure and shape are direct reflections of the dark energy (e.g. Bos et al. 2012).

One of the most striking features of the cosmic web are the elongated matter

flows, filaments. Filaments connect the knots and bind the cosmic web together. They are believed to act as the highways of the universe, transporting matter into cluster environments (van Haarlem & van de Weygaert 1993; Knebe et al. 2004). Typically filaments are under 60 Mpc long and have the width of a few megaparsecs (Aragón-Calvo et al. 2010; Tempel et al. 2014b). One of the largest known filaments in the local universe is the $130h^{-1}$ Mpc long Pisces-Pegasus filament (Batuski & Burns 1985), which is part of the Perseus-Pisces complex (Haynes & Giovanelli 1986). While voids occupy a large fraction of the universe's volume but contain only a relatively small fraction of the total mass, filaments are the opposite; they fill $\sim 10\%$ of the volume but contain about a half of the total mass of the universe (Cautun et al. 2014). Although filaments are generally denser environments than voids and walls, they can be found at a wide span of large-scale densities, from voids to supercluster environments (Aragón-Calvo et al. 2010; Einasto et al. 2012; Alpaslan et al. 2014b). Hydrodynamical simulations predict that a considerable fraction of the missing baryons are located in filaments in the form of a diffuse gas (Tuominen et al. 2021).

3.2 Finding filaments

The characterisation and extraction of the morphological features of large-scale structures and filamentary network is challenging due to the complex geometry and intrinsic multiscale nature of the cosmic web. For this purpose, several techniques have been developed. The methods can be broadly divided into six categories and each of them have their own strengths and weaknesses. These methods are briefly presented below, a more detailed description and comparison of some of the methods can be found in Libeskind et al. (2018).

Early attempts to extract the cosmic web were made by percolation analysis (Zel'dovich et al. 1982) and the minimal spanning tree method using particle dis-

tribution (Barrow et al. 1985). Since then graphical techniques have advanced for example with the adapted minimal spanning tree method developed for identifying filaments and voids in the GAMA survey (Alpaslan et al. 2014a).

Most frequently used techniques are the geometric methods. In these methods the morphology of the web is determined by computing the Hessian of the density, tidal or velocity shear fields (e.g. Aragón-Calvo et al. 2007; Hahn et al. 2007; Hoffman et al. 2012). This can be done using fixed smoothing scale or the scale-space multiscale methods, e.g. the NEXUS+ method (Cautun et al. 2013).

Topological techniques find cosmic web elements by the connectivity and topological properties of the field by implementing the Morse theory. As an instance of such formalism is the Spineweb method (Aragón-Calvo et al. 2010), that extends the watershed transform based void finder (Platen et al. 2007) to trace also filaments, knots and sheets.

Phase space techniques describe the evolving matter distribution as a folding 3D sheet that does not cross itself in the 6D position-velocity phase space. As an example of these techniques are the ORIGAMI method (Falck et al. 2012; Falck & Neyrinck 2015) and the phase-space sheet methods (e.g. Shandarin 2011).

A promising way to identify cosmic web components is by machine learning algorithms. Aragón-Calvo (2019) characterised filaments and walls by a deep convolutional neural network with a U-Net architecture that was trained with a Voronoi model and a geometric method to detect the cosmic web.

Stochastic techniques identify structures by statistically evaluating stochastic processes applied on galaxy or halo distribution. One of the methods belonging to this class is the Bisous method (Stoica et al. 2005; Tempel et al. 2014b; Tempel et al. 2016). The filaments studied in this thesis are extracted from the EAGLE galaxy distribution using the Bisous method. The filament catalog is made by Ganeshaiah Veena et al. (2019).

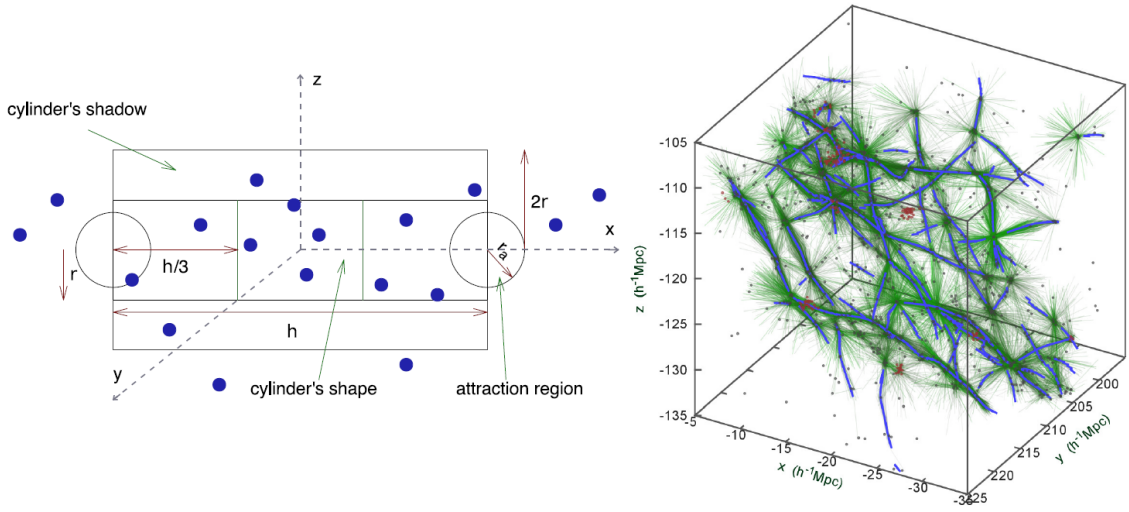

Figure 3: Left panel: a two-dimensional projection of a cylinder and the cylinder's shadow fitted in a pattern of galaxies (points) in the Bisous method. The shown model parameters are the cylinder radius r, cylinder length h and the radius r_a of the attraction region. Right panel: cylinders from several MCMC runs (green lines), extracted filament spines (blue lines) and galaxies (red and grey points). Figure adapted from Tempel et al. (2014b).

3.2.1 The Bisous method

The Bisous method (Stoica et al. 2005; Tempel et al. 2014b; Tempel et al. 2016) approximates the filamentary network by small connected and aligned cylinders. The model is based on a marked point process. A marked point process is a point process where an additional mark is designated to every point. In the case of the Bisous model, cylinder centers are treated as points and marks are associated with the cylinder radius r, length h and orientation.

The cylinders are fitted to the galaxy distribution such that the galaxies inside the cylinder outnumber the galaxies inside the cylinder "shadow", which is obtained by subtracting the initial cylinder from a bigger one. An attraction region is used to link cylinders together to form longer chains. The cylinders are linked together if they are well aligned and separated by distance less than the attraction radius r_a. The left panel of Figure 3 illustrates the cylinder and the different parameters.

The cylinder fitting is done with multiple Markov chain Monte Carlo (MCMC) simulations. The filamentary structure is extracted by finding the points with the highest probability belonging to a filament. These spine points with fixed separation distance define the axis of the filament, the filament spine. The right panel of Figure 3 illustrates the multiple MCMC runs and the emerging filament spines. The benefit of this method is that it can be easily applied to observations since it does not require density field reconstruction as the filaments can be extracted directly from the galaxy distribution either in observational or simulated data.

3.3 Impact of the cosmic web

The large-scale structure of the expanding universe evolves under the laws of gravity, galaxies and dark matter intertwined in the cosmic web. Thus the relationship between galaxies and the cosmic web provides insight on the underlying cosmology and the formation and evolution of galaxies.

It could be argued that the main factor in determining the intrinsic properties of a galaxy is the dark matter halo environment where the galaxy is formed, as the halo mass is found to correlate with many galaxy properties, such as stellar mass, specific star formation rate, color and morphology (Weinmann et al. 2006; Behroozi et al. 2010; Wilman & Erwin 2012).

However, galaxies are known to have different intrinsic properties depending on the large-scale environment they are embedded in. The morphology–density relation implies that dense cluster environments are populated with early-type elliptical and S0 galaxies, while late-type spiral galaxies are more likely to be found in voids (Dressler 1980). Several observational studies show a connection between the large-scale environment and galaxy properties other than the morphology (Lietzen et al. 2012; Einasto et al. 2014; Luparello et al. 2015). Moreover, with fixed mass older dark matter halos seem to be clustered more strongly than halos formed more

recently. This effect, known as the assembly bias, suggests that the large-scale environment and galaxy properties are related to each other (Gao et al. 2005). How much of the galaxy properties are determined by nature and how much by nurture, is still an open question.

Filaments are a distinct environment of the cosmic web with their own dynamics and matter flows (Ebeling et al. 2004; Colberg et al. 2005; Tempel et al. 2014a). Therefore effects on the galaxy properties would be expected. As mentioned in section 3.1, filaments are generally denser environments than voids and walls, but can be found in low-density void regions as well in dense superclusters, making the effects arising from density alone difficult to disentangle.

One of the recognised effects of filaments on the their galaxies is the alignment of galaxy axes. According to the tidal torque theory (Hoyle 1951; Peebles 1969; Doroshkevich 1970), the rotation of halos and galaxies originates from the tidal torques induced by the inhomogeneous density field. The same tidal forces are also responsible for the anisotropic collapse of the surrounding matter. Thus the alignment between galaxy spins and filaments can be expected. The spin axis of spiral galaxies and the longer axis of elliptical galaxies are observed to align with filaments (Tempel et al. 2013; Tempel & Libeskind 2013; Hirv et al. 2017). The alignment has also been found in galaxy pairs and larger satellite systems (Tempel & Tamm 2015; Tempel et al. 2015). Several of these studies propose that the morphology or mass dependent alignment could be explained through different mass accretion history. After collapsing, galaxies can acquire angular momentum through mergers, flybys and accretion. The tidal torquing also continues, but at much lower rate. Spiral galaxies accrete mass smoothly, and retain their original spin when migrating from sheets to filaments. On the other hand, elliptical galaxies have undergone major mergers. These mergers could occur preferentially parallel to filaments, as the velocity field in filaments is suggested to be aligned with the filament spine (e.g.

Tempel et al. 2014a). Thus, more massive galaxies acquire more perpendicular spin alignments.

In general, the filament galaxies are observed to be more massive, redder and less star forming than the galaxies outside and that these properties depend on the distance to the filament spine (Kuutma et al. 2017; Poudel et al. 2017; Laigle et al. 2018; Sarron et al. 2019). In addition, the HI content of filament galaxies is found to increase with the distance from the filament spine (Crone Odekon et al. 2018) and Hα-emitting clouds found in the outskirts of filament galaxies could indicate that filaments shape the gas content of their galaxies (Vulcani et al. 2019). Numerical simulations suggest that the galaxy quenching originates from the local web environment, as galaxies stop accreting gas when they detach from the surrounding environment (Aragón-Calvo et al. 2019). Also the halo mass function is shown to evolve distinctly depending on the web environment (Cautun et al. 2014).

Still controversy exists regarding on the influence of the filament environment on the galaxy properties. Some studies suggest that the local, group environment is the only factor that affects the galaxy intrinsic properties. Eardley et al. (2015) found that local density is responsible for the changes in galaxy luminosity functions in different large-scale environments. Brouwer et al. (2016) found no correlation between average halo mass of central galaxies and their cosmic web environment. Kuutma et al. (2020) found no change in galaxy properties as a function of the distance from filament spines, concluding that the intrinsic properties depend only on the local density. From simulation data Goh et al. (2019) found that at fixed environmental density the cosmic web does not affect the shapes or mass accretion of dark matter halos.

In the past literature, the non-linear 3D peculiar velocities have not been much studied in the cosmological scale, as they cannot be measured from observations. However, in the linear regime, the bulk velocities in the local universe are thoroughly

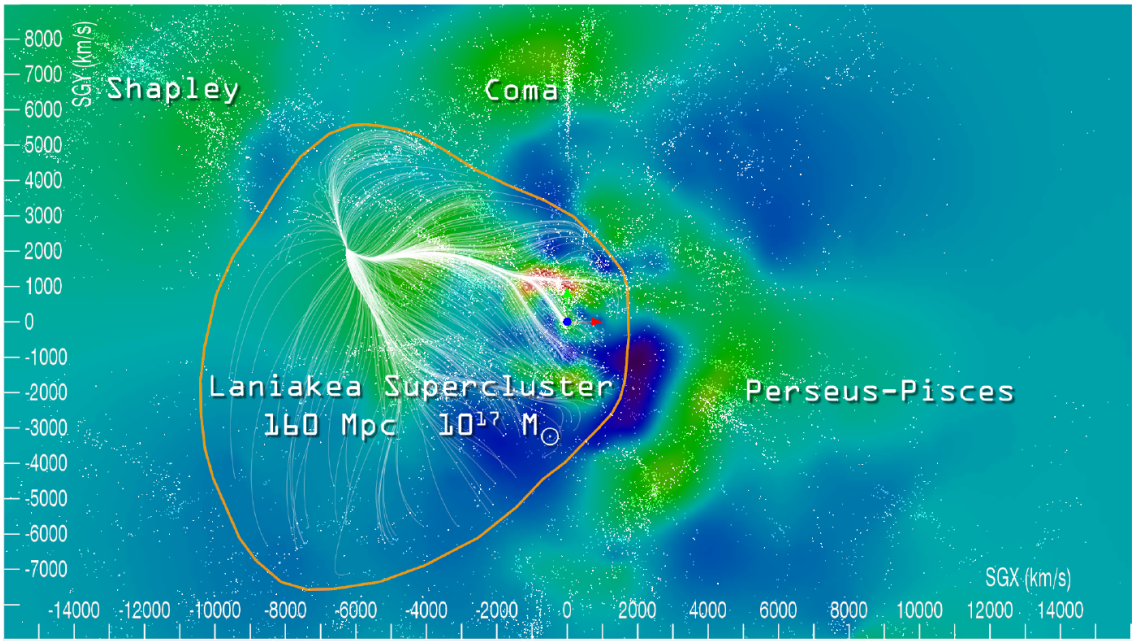

Figure 4: A slice of the Laniakea supercluster, shown in orange line, in the supergalactic equatorial plane. Velocity streams within the Laniakea are shown in white lines and galaxies as white dots. The blue dot is the Milky way. Colored regions represent density values (Tully et al. 2014).

mapped. Linear bulk velocities can be traced down to scales of a few Mpc due to the simple relation between the velocity and density fields defined in the equation (23). Our home supercluster, the Laniakea, is defined with the observational Cosmicflows-2 data (Tully et al. 2013). This data is a compilation of radial peculiar velocities and distances measured with different methods for over 8000 galaxies. In Figure 4 the orange line represents the edges of the Laniakea, where the only velocity component is the Hubble flow.

In several theoretical studies, velocity fields are found to be parallel with filament spines (Sousbie et al. 2008; Tempel et al. 2014a; Kraljic et al. 2019; Pereyra et al. 2020). In general, dark matter halos in numerical simulations are also found to have parallel motions. Trowland et al. (2013) found that halos in filaments defined with the density field have parallel motions and that the motion is the most parallel for massive halos. Forero-Romero et al. (2014) showed that halos below masses

$\sim 10^{13} h^{-1} \mathrm{M}_{\odot}$ tend to move along filaments defined with the tidal and velocity shear fields, but do not separate between filament and wall halos. Ganeshaiah Veena et al. (2018) obtained similar results, showing that simulated halos inside of filaments based on the NEXUS method flow preferentially along the filaments. These studies do not however compare the peculiar motions inside and outside of filaments and they concern only dark matter halos.

In this thesis the peculiar motions of galaxies inside of filaments and in their immediate vicinity are studied. For this purpose, filaments made with the Bisous method are used. The Bisous method is based on the distribution of galaxies, unlike many other filament finding methods that use some kind of smoothing over a field. It is thus natural to focus on the motions of individual galaxies. The study of galaxy motions enables the analysis of the individual features, such as the galaxy properties and the distribution of galaxies inside of filaments, information that would be otherwise lost.

4 Analysis and results

The aim of this thesis is to find answers to the following questions:

- Does the peculiar velocity magnitude and direction of galaxies inside of filaments differ from those on the outside?
- Does the peculiar velocity magnitude and direction depend on the geometric properties of filaments?
- Is the peculiar motions of galaxies inside of filaments connected to the galaxy properties?

In the subsequent analysis, these questions are studied with the data introduced in the next section. Through the analysis the value of the Hubble constant $h = 0.68$ is used.

4.1 The data

The galaxies studied are from the EAGLE simulation Ref-L0100N1504 (Table II) at $z = 0$. The parameters selected from the simulation for each galaxy are the peculiar velocity vector components, coordinates, group mass M_{200}, stellar mass $M_\star$, star formation rate (SFR), age and dust corrected magnitudes in the g- and r-band. For the stellar mass and star formation rate the values within a 30 kpc aperture are used to match observational measurements. In the simulations magnitudes are calculated for galaxies with more than 100 star particles. From this follows a lower limit for the galaxy stellar mass, $M_\star > 1.58 \times 10^8 \mathrm{M}_\odot$.

The filamentary structure used to identify filament galaxies is extracted by Ganeshaiah Veena et al. (2019) using the Bisous method (described in section 3.2.1) on the distribution of EAGLE galaxies with total stellar masses above $10^8 h^{-1} \mathrm{M}_\odot$. The parameters used from this filament catalog are the filament identification number, filament spine point coordinates, number of spine points within a filament, filament radius at each spine point, galaxy's nearest spine point identification number, galaxy's perpendicular distance to the filament spine D_{fil} and the luminosity density field of galaxies ρ. The luminosity density field is the galaxy number density field measured within a chosen smoothing radius and multiplied by galaxy luminosities. Figure 5 shows the spatial location of central galaxies in a 10 Mpc slice with the color contours illustrating the luminosity density field of galaxies with a 8 Mpc smoothing radius interpolated linearly on a grid.

In this work, the parameters calculated using the filament data are the filament spine vector $\mathbf{s}$, alignment angle θ between the filament spine vector and the galaxy velocity vector, filament length L_{fil}, filament radius R_{fil}, parallel distance l_{fil}, normalised parallel distance $l_{\mathrm{fil}}/L_{\mathrm{fil}}$ and normalised perpendicular distance $R_{\mathrm{fil}}/D_{\mathrm{fil}}$. Figure 6 shows a schematic presentation of a filament with the related parameters.

In general, filaments shorter than 5 Mpc reside inside cluster or void environ-

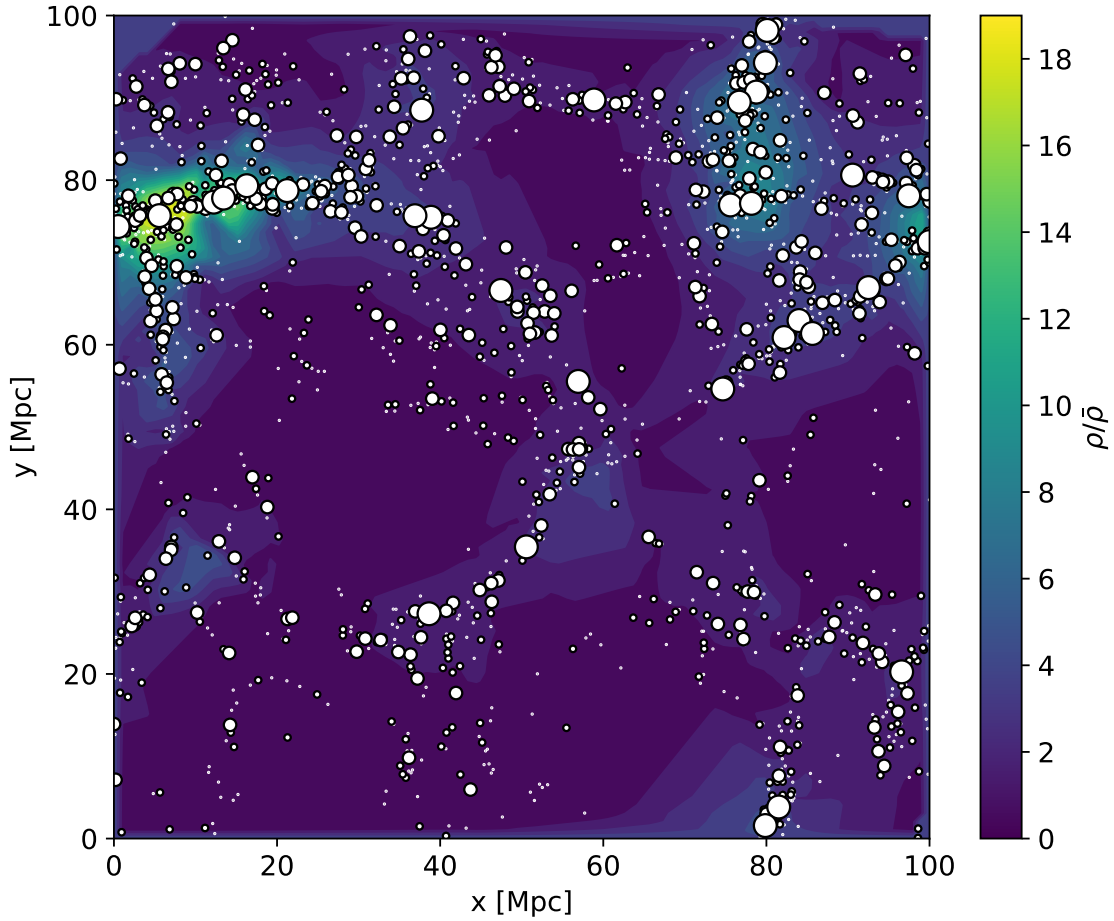

Figure 5: A 10 Mpc slice from the EAGLE Ref-L0100N1504 simulation with central galaxies and galaxy luminosity density field ρ with a 8 Mpc smoothing radius in units of the mean luminosity density $\bar{\rho}$. The size of the circle scales with galaxy's stellar mass in four intervals: $M_\star/\mathrm{M}_\odot = 10^8 - 10^9$, $10^9 - 10^{10}$, $10^{10} - 10^{11}$ and $10^{11} - 10^{12}$.

ments (Kuutma et al. 2020). In clusters the galaxy velocities and properties are under the influence of the cluster environment. In voids the detected filaments are uncertain, result from the low number of galaxies. Thus, to attain an uniform sample, filaments shorter than 5 Mpc and galaxies for which the closest filament is such, are excluded from the analysis. Within the EAGLE simulation the Bisous method finds 305 filaments that are longer than 5 Mpc.

Following the same reasoning as above, galaxies that have a filament endpoint as

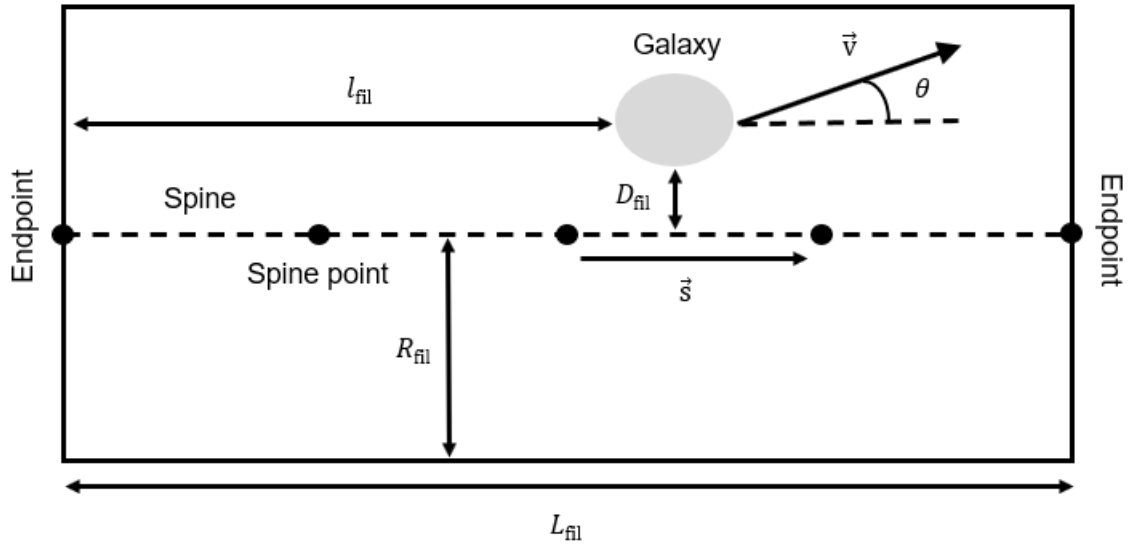

Figure 6: A schematic illustration of a filament and the parameters used in this work: peculiar velocity vector $\mathbf{v}$, filament spine vector $\mathbf{s}$, alignment angle θ, filament length $L_{\rm fil}$, parallel distance $l_{\rm fil}$, filament radius $R_{\rm fil}$ and perpendicular distance $D_{\rm fil}$.

the nearest spine point are removed, as they are typically located in clusters. The exclusion of these galaxies still leaves a handful of rather massive halos. The median peculiar velocities of satellite galaxies within groups with halo mass $M_{200} > 10^{14}\mathrm{M}_{\odot}$ are near or over 1000 km/s, which is considerably higher than for lower mass groups, where the velocities are under 700 km/s. Thus, halos with $M_{200} > 10^{14}\mathrm{M}_{\odot}$ are considered as clusters and removed.

To compare galaxies inside and outside of filaments, the data is divided into in and out samples by the filament radius. The filament radius $R_{\rm fil}$ is defined individually to each filament as the median of the spine point cylinder radii. The outside region is defined as a region from $R_{\rm fil}$ to 4 Mpc. The outer limit of 4 Mpc is chosen as beyond this the median luminosity density field of galaxies decreases, indicating a separation between void and other large-scale environments (Kuutma et al. 2020).

In this thesis the peculiar motions of central galaxies are studied. Satellite galaxies are omitted as they strongly reflect also the host group's gravitational potential,

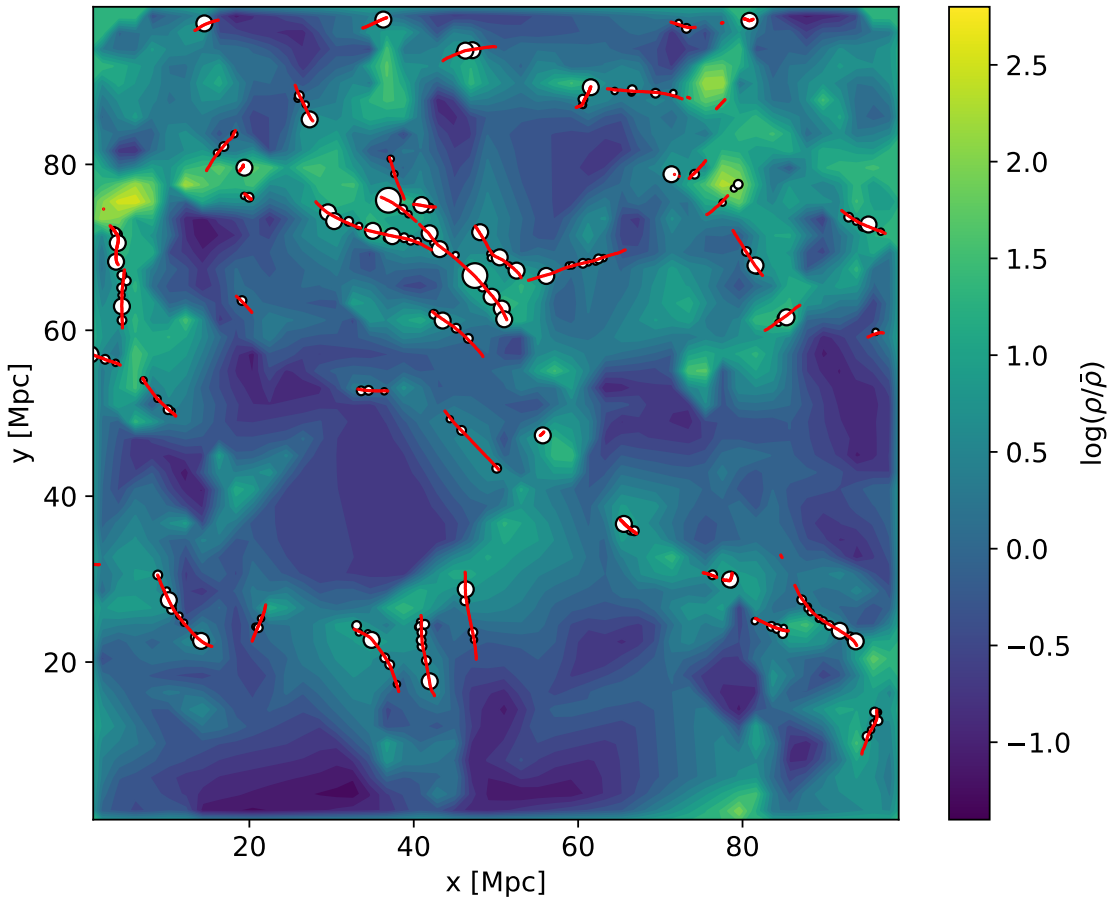

Figure 7: Filaments longer than 5 Mpc (red lines), central galaxies inside of the filaments (white circles) and galaxy luminosity density field ρ with a 2 Mpc smoothing radius in units of the mean luminosity density $\bar{\rho}$, in the same 10 Mpc slice as in Figure 5. The circle size scales with galaxy's stellar mass in the same mass intervals as in Figure 5.

causing rotational motions. The peculiar motions of groups with more than two galaxies do not differ much from the motions of the central galaxies. Only 7% of the groups have peculiar velocities and alignment angles that differ from those of the central galaxies more than 20%. In a way, a central galaxy tracks the peculiar motion of the group, as they are located at the minimum of the group's gravitational potential.

Applying the above limits to the data, the final sample contains 1665 central galaxies inside of filaments, while the outside region has 1810 central galaxies. The

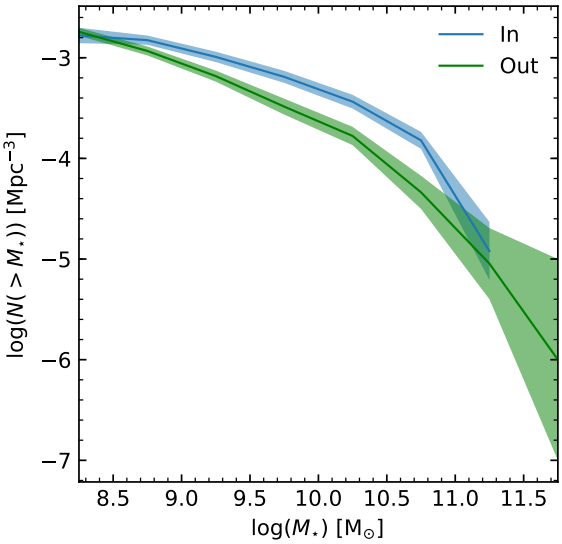

Figure 8: Stellar mass function of central galaxies inside (blue) and outside (green) of filaments.

spines of filaments and the central galaxies inside the filaments are shown in Figure 7 in the same slice as in Figure 5.

The central galaxy stellar mass function is shown in Figure 8 with Poisson error limits. In the mass range $10^{8.5}M_{\odot}$ – $10^{11}M_{\odot}$ and with fixed cumulative number density, the filament galaxies are more massive than on the outside. This is consistent with the observations of filament galaxies being more massive (Poudel et al. 2017; Laigle et al. 2018). The cosmic web environments defined with the NEXUS+ method from the EAGLE data also shows that the majority of galaxies that are more massive than $\sim 10^{9}M_{\odot}$ are located in filaments (Ganeshaiah Veena et al. 2019). Table III lists the galaxy counts within 1 dex stellar mass and group mass intervals.

Table III: Central galaxy counts inside and outside of filaments in galaxy stellar mass $M_\star$ and group halo mass M_{200} intervals.

$M_\star[\mathrm{M}_\odot]$	N_{in}	N_{out}
10^8 – 10^9	645	1153
10^9 – 10^{10}	654	490
10^{10} – 10^{11}	354	158
10^{11} – 10^{12}	12	9

$M_{200}[\mathrm{M}_\odot]$	N_{in}	N_{out}
10^9 – 10^{10}	0	3
10^{10} – 10^{11}	506	895
10^{11} – 10^{12}	936	826
10^{12} – 10^{13}	209	77
10^{13} – 10^{14}	14	9

4.2 Peculiar motions inside and outside of filaments

In the EAGLE simulations, the peculiar velocity components of a galaxy are defined as the peculiar velocity of the galaxy's center of mass,

$$\mathbf{v}_x \equiv a\dot{\mathbf{x}} = a\frac{\sum_i m_i\dot{\mathbf{x}}_i}{\sum_i m_i} \qquad \mathbf{v}_y \equiv a\dot{\mathbf{y}} = a\frac{\sum_i m_i\dot{\mathbf{y}}_i}{\sum_i m_i} \qquad \mathbf{v}_z \equiv a\dot{\mathbf{z}} = a\frac{\sum_i m_i\dot{\mathbf{z}}_i}{\sum_i m_i}, \tag{31}$$

where a is the scale factor, m is particle mass including all particle species belonging to the galaxy, $\dot{\mathbf{x}}$, $\dot{\mathbf{y}}$ and $\dot{\mathbf{z}}$ are the time derivatives of the comoving coordinates of the galaxy's center of mass taking into account periodic boundary conditions. The 3D peculiar velocity vector is the sum of all its components,

$$\mathbf{v}_{\mathrm{pec}} = \mathbf{v}_x + \mathbf{v}_y + \mathbf{v}_z. \tag{32}$$

It should be noted that the linear velocity induced by scales larger than the simulation box given by the equation (27) should be added to the peculiar velocities to obtain the precise magnitude of the velocity. This is not done in this thesis. Thus the focus is not on the velocity magnitudes, but on the change in them.

The direction of a galaxy's peculiar motion is calculated in respect to the filament spine vector $\mathbf{s}$ between the two closest spine points (cf. Figure 6) and represented by the alignment angle θ,

$$\theta = \cos^{-1}\left(\left|\frac{\mathbf{v}_{\mathrm{pec}}\cdot\mathbf{s}}{\|\mathbf{v}_{\mathrm{pec}}\|\|\mathbf{s}\|}\right|\right). \tag{33}$$

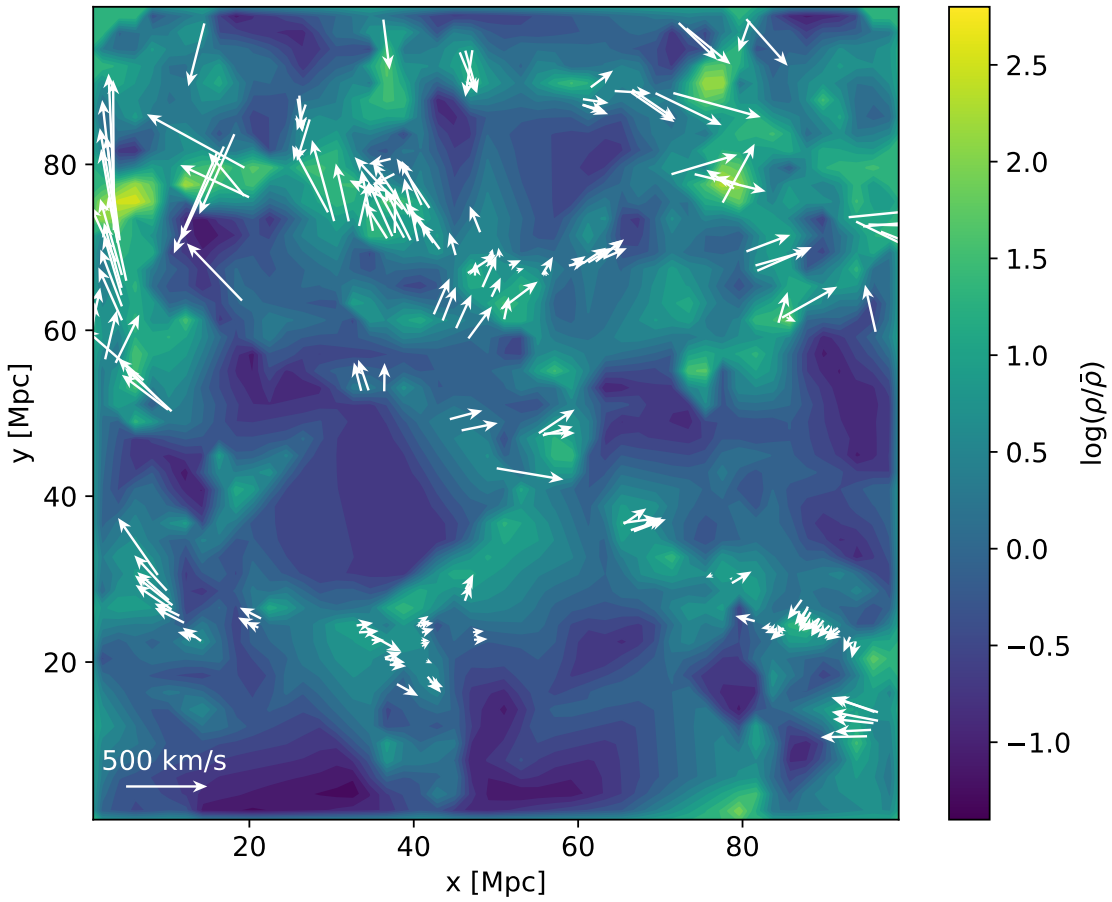

Figure 9: Two-dimensional peculiar velocity vectors of filament central galaxies seen in Figure 7 in the same 10 Mpc slice and with the same luminosity density field.

With this definition the alignment angle is between 0 and 90 degrees. Motion is more parallel to the filament spine when the angle is < 45 degrees and more perpendicular at > 45 degrees. The 2D peculiar velocity vectors for the same central galaxies as in Figure 7 are shown in Figure 9. The galaxies with the highest velocities are near regions where the luminosity density is the highest, showing that also in the non-linear regime the velocities strongly follow the matter distribution.

The left panel of Figure 10 shows the peculiar velocity function of the central galaxies inside and outside of filaments with Poisson error limits. At fixed cumulative number density and without errors, filament galaxies have lower velocities than the

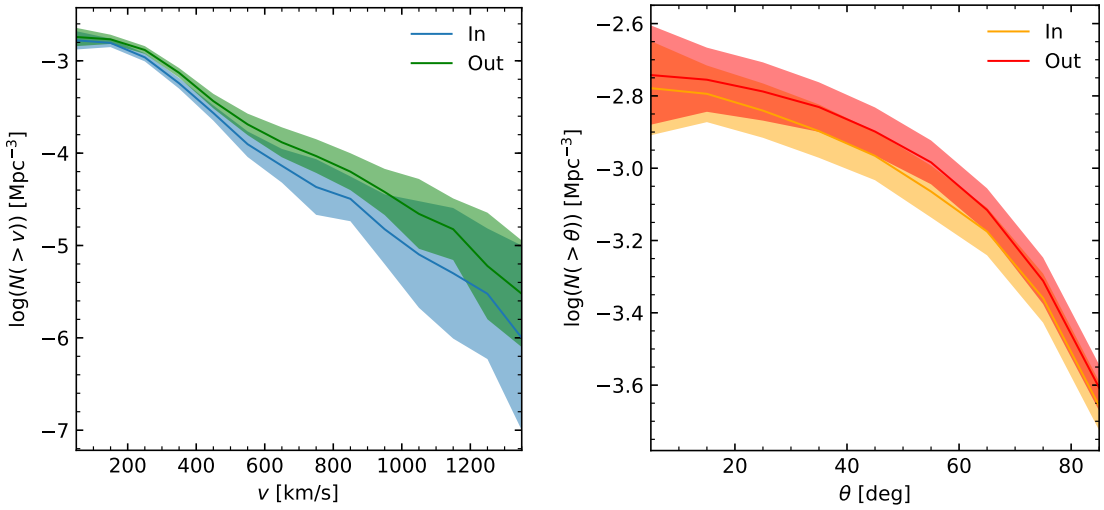

Figure 10: Left panel: peculiar velocity function of central galaxies inside (blue) and outside (green) of filaments. Right panel: alignment angle function of central galaxies inside (yellow) and outside (red) of filaments.

ones on the outside. The right panel shows the alignment angle function of the central galaxies with Poisson errors. Inside of filaments, the peculiar velocities are directed more parallel to the filament spines than on the outside (without errors). Similar motions has been seen in the velocity field of dark matter particles (Pereyra et al. 2020). The median peculiar velocities and alignment angles inside and outside of filaments are listed in Table IV.

To check the similarity of the distributions inside and outside of the filaments a two-sample Kolmogorov-Smirnov (KS) was run for the galaxy stellar mass, the peculiar velocity and the alignment angle distributions with a Gaussian smoothing. The KS test is a measure of the likelihood that two samples are drawn from the same distribution. The test result, the p-value, is typically less than 0.05 for unidentical samples. The p-values for the tested distributions are all $p \ll 0.01$, which are low enough to say that the samples are not drawn from the same distribution.

In the following analysis all measured values are shown as median values. The median values and error limits are estimated with the bootstrap resampling method,

Table IV: The median peculiar velocity and alignment angle between the velocity vector and filament spine of central galaxies inside and outside of filaments.

	In	Out
v [km/s]	242	267
θ [degrees]	51	55

which is best suited for a small sample size. With this method galaxies in bins with equal width are drawn randomly with replacement creating new samples with the same number of data points as in the original bin. This process is repeated 1000 times. From these new samples the median values and error limits as $\pm 1\sigma$ are measured for each bin. Only bins with 5 or more central galaxies are shown.

Figure 11 shows the galaxy peculiar velocities as a function of the alignment angle. In general, the velocities rise as the alignment becomes more parallel to the spines. The high velocities of parallelly aligned galaxies could be due to galaxy flows aligning towards the clusters at the endpoints of the filaments, while the galaxies at higher angles have not yet adjusted to the flow and have more randomised motions. An exception in this are the most parallelly moving outside galaxies, for which the velocities can be lower than on the inside. This could be due to very local gravitational effects, which can be expected to be seen when studying the peculiar motions of individual galaxies.

The difference in velocities between galaxies inside and outside of filaments is also seen in Figure 12 left panel, where the median peculiar velocity of central galaxies with fixed group mass is shown. In the mass range $10^{10.5-12}\mathrm{M}_{\odot}$ the velocities are lower inside than outside of the filaments. In addition, in each mass bin the median velocity without errors is lower for galaxies inside of filaments. This could be the result of filaments being in general more denser environments than the surroundings (Aragón-Calvo et al. 2010; et al. 2014), which is supported by the mass distribution

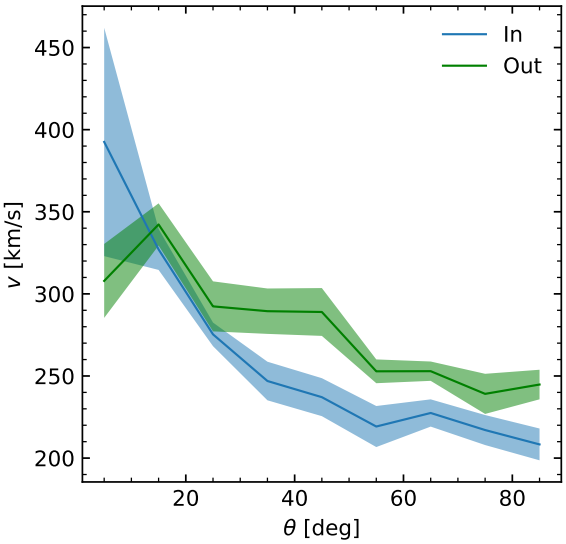

Figure 11: The median peculiar velocity of central galaxies as a function of the alignment angle inside (blue) and outside (green) of filaments.

seen in Figure 8. Galaxies in denser environments inevitably experience more interactions, such as flybys, smooth accretion and mergers. These same processes are partly behind the alignment of galaxy spins seen in filaments (Tempel et al. 2013; Tempel & Libeskind 2013; Hirv et al. 2017). Galaxies in filaments could be moving slower as part of the kinetic energy associated with the translational motion is converted into the galaxy's angular momentum.

There is a clear inverse relation between the velocities and the group mass at masses between $10^{10}M_{\odot}$ and $10^{12.5}M_{\odot}$, both inside and outside of filaments. This could also be explained through the increased rate of interactions. More massive groups have been more influenced by different interactions throughout their formation history.

The alignment angle of central galaxies is shown in Figure 12 right panel. Between masses $10^{10}M_{\odot}$ and $10^{11.5}M_{\odot}$, the galaxy motions inside of filaments are more aligned with the filament spines than on the outside. Without errors, the median angle at fixed mass is smaller in filaments, which was also seen in the distribution of

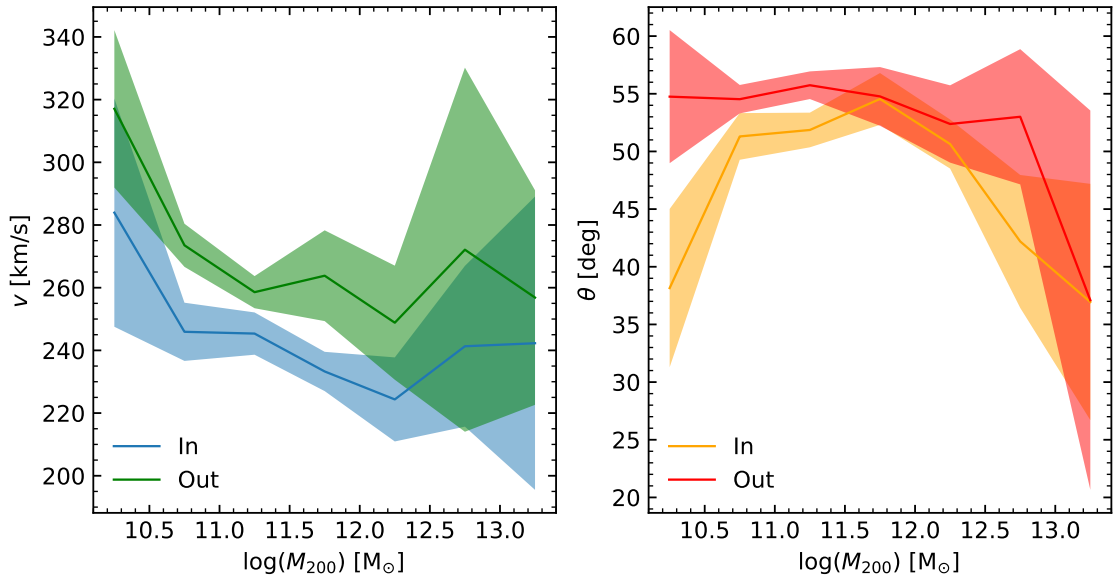

Figure 12: Left panel: the median peculiar velocity of central galaxies as a function of group mass inside (blue) and outside (green) of filaments. Right panel: the median alignment angle of central galaxies as a function of group halo mass inside (yellow) and outside (red) of filaments.

alignment angles in Figure 10. In general, the galaxies inside of filaments are moving more parallel to the filament spines than the galaxies on the outside. The filament galaxies seem to be flowing towards clusters, while the galaxies on the outside are moving more perpendicular to the filament spine as they are not only streaming towards clusters, but also the filaments.

The galaxies in the most massive groups both inside and outside of filaments generally have more aligned motions than on average, which is in accordance with the results by Trowland et al. (2013). These are one of the oldest galaxies in the sample. The parallel alignment inside of filaments could be due to that these galaxies have had more time to adjust to the flow towards clusters. On the outside, some of these galaxies seem to also be heading towards a cluster, moving parallelly to the filaments rather than collapsing onto the filaments. In general, the motion of galaxies in the most massive groups both inside and outside of filaments seems to be dominated by the attraction from the filament endpoint clusters as there is no larger

matter concentration nearby. The galaxies in low mass groups inside of filaments also have parallel motions. This may be the consequence of a local flow. A nearby more massive group could induce motions differing from the general flow. Although the motions are more parallel inside of the filaments, the alignments are still slightly perpendicular in the mass range $10^{10.5-12.5}\mathrm{M}_{\odot}$, which is in conflict with previous studies finding parallel motions (Forero-Romero et al. 2014; Ganeshaiah Veena et al. 2018). This could indicate different flows emerging in filaments identified with different methods, as seen in Forero-Romero et al. (2014). The filament properties in general are found to be dependent on the identification method (Rost et al. 2020).

In general, group mass seems to affect peculiar motions through the rate of experienced interactions increasing with increasing group mass. As the galaxy properties are also known to correlate with the local, group environment, to study the effects of filament environment and galaxy properties on the peculiar motions it is essential to fix the dark halo mass. In the following sections the group mass is fixed in four bins; $10^{10-11}\mathrm{M}_{\odot}$, $10^{11-12}\mathrm{M}_{\odot}$, $10^{12-13}\mathrm{M}_{\odot}$ and $10^{13-14}\mathrm{M}_{\odot}$.

4.3 Peculiar motions and filament properties

In this section the relations between the central galaxy peculiar motions and geometric properties of the filaments are studied. To verify if the results are due to filament-only induced effects or not, these relations are also studied on the outside of filaments. The following analysis is divided into two parts. First is the parallel distances, including the filament length L_{fil}, parallel distance l_{fil} and normalised parallel distance $l_{\mathrm{fil}}/L_{\mathrm{fil}}$. Second is the perpendicular distances, including filament radius R_{fil}, perpendicular distance D_{fil} and normalised perpendicular distance $D_{\mathrm{fil}}/R_{\mathrm{fil}}$.

4.3.1 Parallel distances

The peculiar velocity of galaxies as a function of the filament length is shown in the top panel of Figure 13. The length of a filament is defined to be the distance between the filament endpoints, measured along the filament spine. The galaxy velocities have a turnaround at $\sim$ 15 Mpc. There is a significant increase in the velocities in the last length bin. This is a contribution from a single 31 Mpc long filament, the only filament longer than 25 Mpc in the sample. This filament contains 20 central galaxies in total. The galaxies outside of filaments show a similar trend, with the difference of the velocity minima being in the same length bin for all galaxies in groups with masses below $10^{13}\mathrm{M}_{\odot}$. These calculations were repeated also with a more conservative definition of the outside region to eliminate the possible mixing of inside and outside central galaxies. Still, within the outer region defined as from $2 \times R_{\mathrm{fil}}$ to 4 Mpc, the same trend persists. Thus, the filament length does not only affect the filament galaxy velocities, but also the ones on the outside. The increase of velocity in long filaments is likely due to that longer filaments connect to more massive clusters. Indeed, the longest filament, located in Figure 7 around coordinates (5, 70), is near a large conglomerate of galaxies. The galaxies outside of the filaments also ought to be under the influence of this large gravitating mass, shown by the increase in velocities.

The galaxies in the most massive groups seem to be concentrated in and around of short filaments. This has also been seen through the observations of the fraction of red galaxies increasing in short filaments, as the color tightly correlates with the halo mass (Rost et al. 2020). On the other hand, filaments shorter than 15 Mpc consist 88% of all the filaments within the sample. It could be only because of this that the rare massive groups are nonexistent in long filaments, which are rare objects themselves. Nonetheless, galaxies in the most massive groups are more concentrated in short filaments within the sample. The clusters at the endpoints

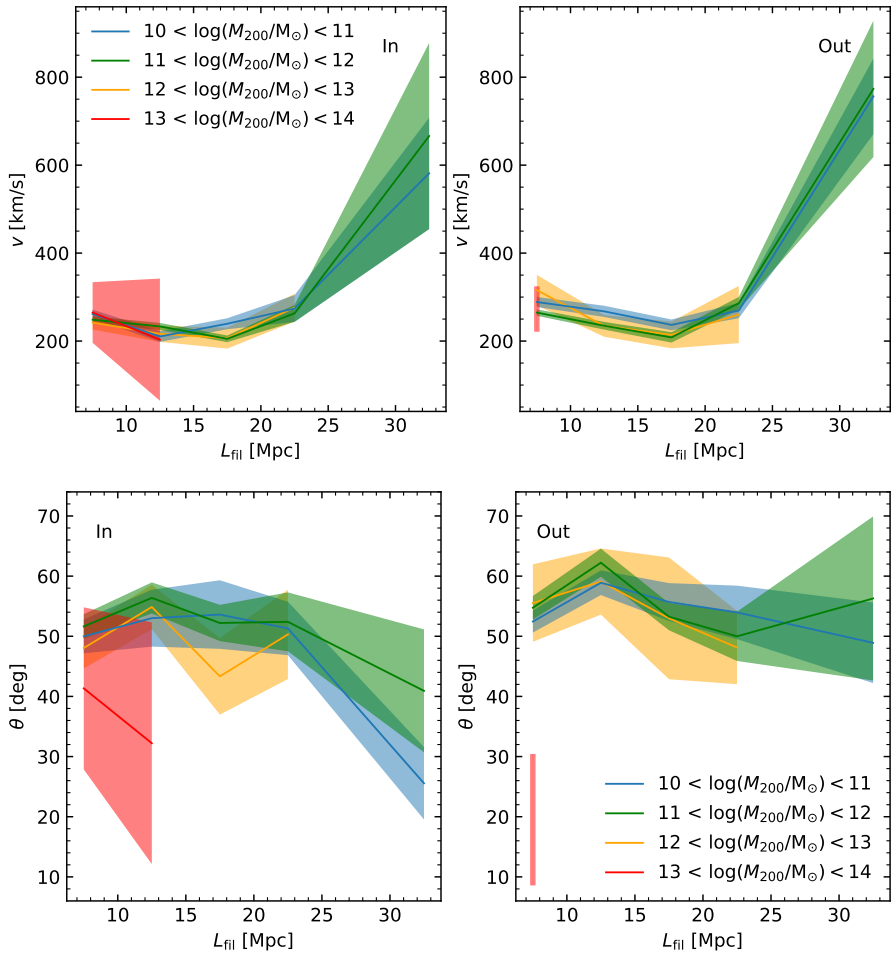

Figure 13: Top panel: the median peculiar velocity of central galaxies as a function of filament length inside (left) and outside (right) of filaments. Bottom panel: the median alignment angle of central galaxies as a function of filament length inside (left) and outside (right) of filaments. Central galaxies are shown with fixed group halo mass.

of these filaments should also be rather massive to be able to retain the elongated galaxy flows towards them. The turnaround in velocities at $L_{\rm fil} \sim 15$ Mpc could suggest that below this limit, the mass of filament endpoint clusters increases with decreasing filament length, while above ~ 15 Mpc the cluster mass increases with filament length.

The long filament has a large cluster only near the other endpoint. Thus the filament length ~ 15 Mpc could also divide filaments into two subgroups; those that have a large cluster at the other endpoint, and to shorter filaments that act

as bridges between two clusters. To confirm this, a further analysis of the filament endpoint environments and cluster connectivity would be needed.

The filament length of ~ 15 Mpc also divides the alignment angles, as seen from the lower panel of Figure 13, matching the general trend of velocities increasing with more parallel alignments seen in Figure 11. In the mass range $10^{10-11}\mathrm{M}_{\odot}$ galaxies have clear parallel motions in the longest filament, as the median angle is under 32 degrees within errors. The parallel alignment is not seen in the galaxies outside of the filament. This shows that in long filaments galaxies can develop coherent and aligned flows, while the outside galaxies do not follow the same motion. The galaxies on the outside are under the effect of cluster gravitation, but at the same time are collapsing towards filaments.

The reason behind that the sample contains only one long filament is the rather small box size of the EAGLE simulation. Filaments longer than 30 Mpc are much more common in observations (Tempel et al. 2014b). It would not be uncommon to choose to study only filaments longer than 30 Mpc. For this a simulation with larger box size would be needed. Because of the 31 Mpc filament being one of a kind specimen in the simulation, Figure 12 and the following analysis were repeated also without this filament to check that any results were not solely caused by this outlier.

The peculiar velocities and alignment angles as a function of the parallel distance are shown in Figure 14. The parallel distance is defined as the distance from a filament endpoint to the galaxy's location, approximated with the location of the nearest spine point. In general, velocities follow a similar trend than in Figure 13, but also some local flows can be seen. On the outside, galaxies in the 25 – 30 Mpc distance bin are concentrated near the endpoint of the longest filament near the massive cluster. Over 60% of the total number of central galaxies outside the longest filament are near the cluster, which explains the high velocities seen also

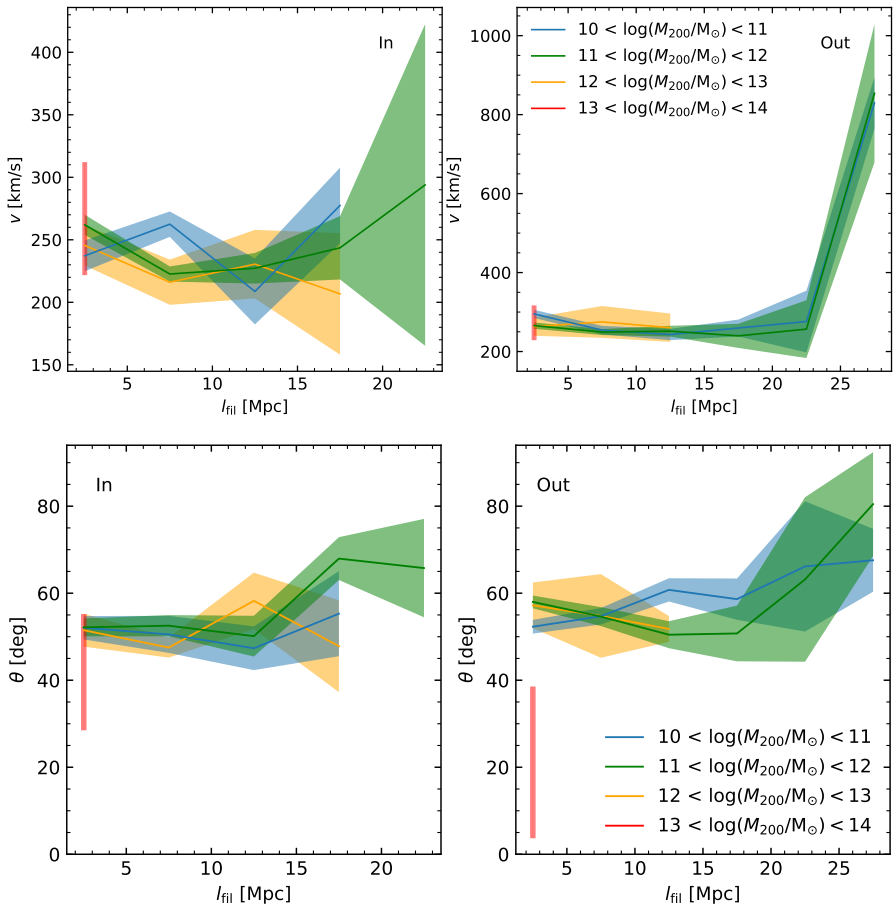

Figure 14: Top panel: the median peculiar velocity of central galaxies as a function of parallel distance inside (left) and outside (right) of filaments. Bottom panel: the median alignment angle of central galaxies as a function of parallel distance inside (left) and outside (right) of filaments. Central galaxies are shown with fixed group halo mass.

in Figure 13. The galaxies inside the longest filament are more spread along the filament.

The lower panel of Figure 14 shows that on the inside of filaments the direction of galaxy peculiar motions are constant along the filament spines in filaments shorter than ~ 15 Mpc. Above this, motions change to more perpendicular direction. This could be the effect of these filaments having a large cluster only at the other filament endpoint. The presence of a massive cluster could induce flows towards different parts of the cluster, rather than a head-on accretion. Highly perpendicular

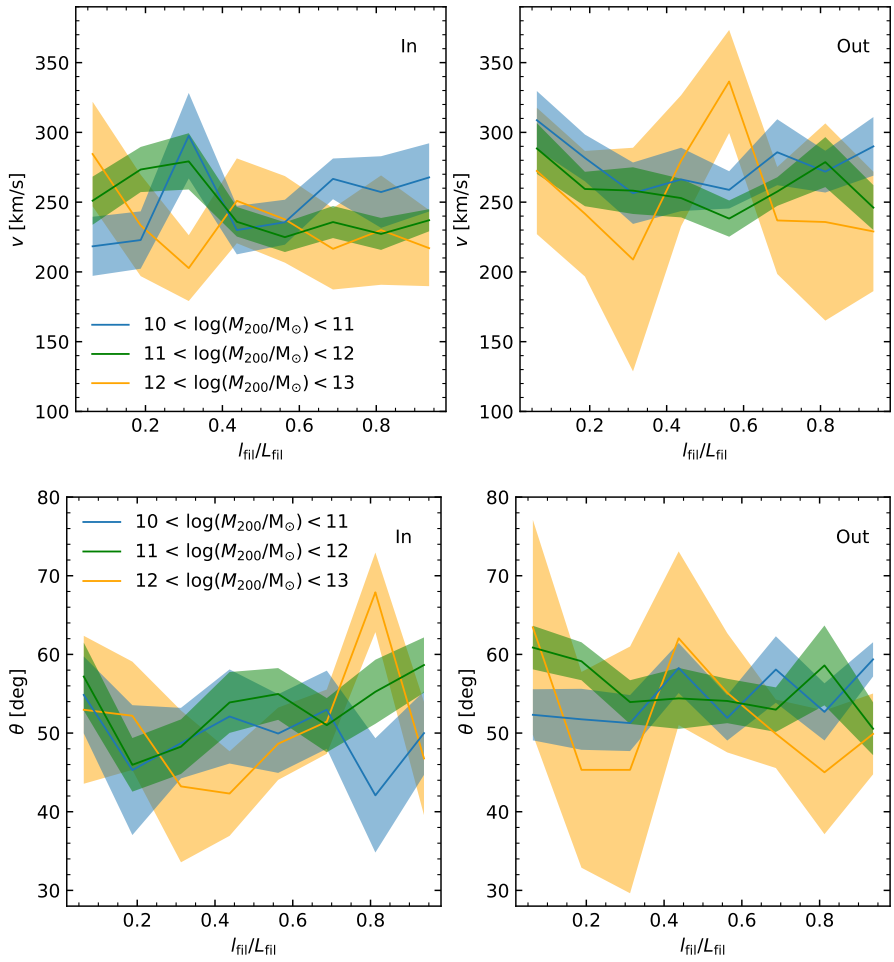

Figure 15: Top panel: the median peculiar velocity of central galaxies as a function of normalised parallel distance inside (left) and outside (right) of filaments. Bottom panel: the median alignment angle of central galaxies as a function of normalised parallel distance inside (left) and outside (right) of filaments. Central galaxies are shown with fixed group halo mass.

motions are also seen on the outside near the other endpoint of the longest filament. These galaxies seem to be falling towards the region where the cluster and filament intersect.

Figure 15 shows the peculiar motions as a function of the normalised parallel distance. Galaxies in the most massive groups are not shown here because of low galaxy numbers in each bin. It is evident that by stacking all the filaments together in each bin, the galaxy motions are highly irregular. This is because the saddle point of a filament, the point where the direction of the velocities diverge in the parallel

direction, can be located at different points along the filament depending on the ratio of the masses of the clusters located at the filament endpoints (Pereyra et al. 2020).

Still, the filament galaxy alignment angles have almost a symmetrical pattern about the center of the filaments in the mass range $10^{10-11}\mathrm{M}_{\odot}$. In the mass range $10^{11-12}\mathrm{M}_{\odot}$ galaxies inhabit a similar pattern, though more diluted and asymmetrical minima around the center. This implies that in general the filaments act as bridges between two almost equal sized clusters. The direction of the flow is what would be expected for filaments acting as cosmic highways, transporting matter into clusters. The galaxy motions diverge at the saddle point and adjust to the flow towards clusters. Near the endpoints, motion changes again to more perpendicular due to cluster accretion.

4.3.2 Perpendicular distances

The peculiar velocity and the alignment angle of galaxies as a function of the filament radius R_{fil} are shown in Figure 16. The filament radius is defined individually to each filament by the median of cylinder radii, from which the filament is constructed in the Bisous method. In the groups with masses higher than $10^{12}\mathrm{M}_{\odot}$ the galaxy velocities are almost constant within errors. In low mass groups, there is a clear decrease in galaxy velocities with filament radius. The decrease is also seen with galaxies in the mass range $10^{11-12}\mathrm{M}_{\odot}$ below 0.65 Mpc, while above this the increase is significant. The irregularities seen in velocities and alignments are probably due to local interactions, rather than a general trend. On the outside of filaments with radius below 0.7 Mpc motions are much more constant, probably as the galaxy number densities and interaction rates might be lower.

The perpendicular distance D_{fil} is defined as the distance from the filament spine to the galaxy position, measured towards the filament radius and beyond. As a func-

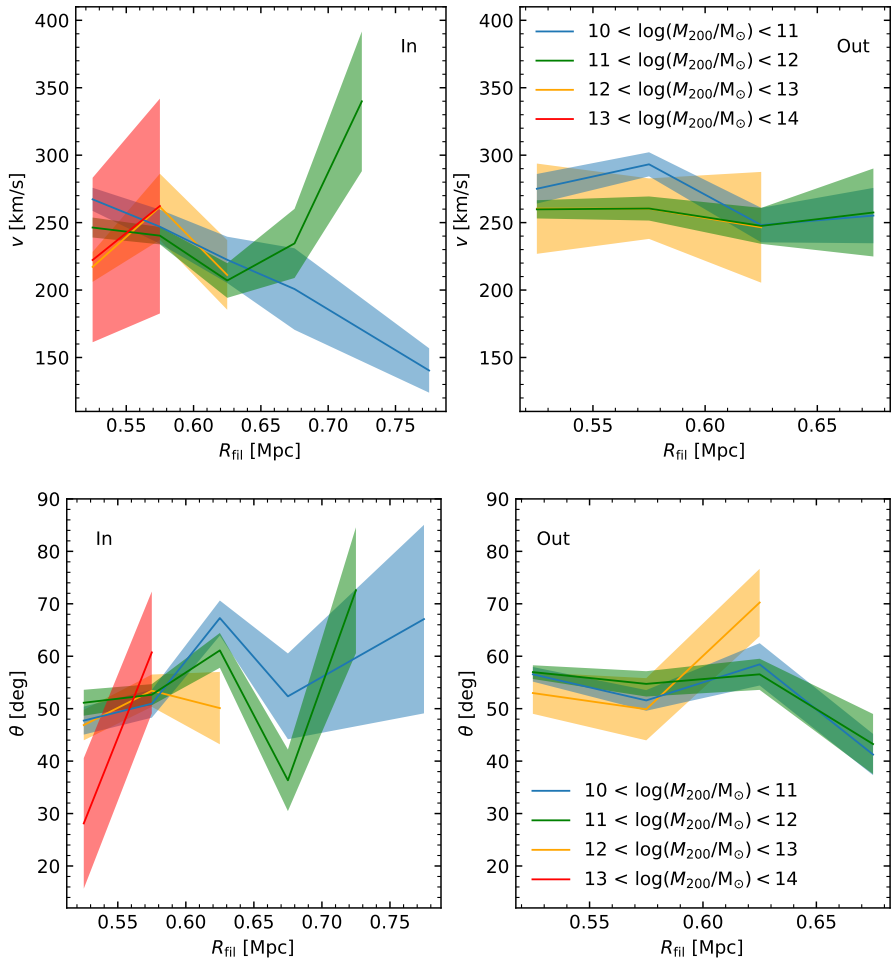

Figure 16: Top panel: the median peculiar velocity of central galaxies as a function of filament radius inside (left) and outside (right) of filaments. Bottom panel: the median alignment angle of central galaxies as a function of filament radius inside (left) and outside (right) of filaments. Central galaxies are shown with fixed group halo mass.

tion of this, the velocity of filament galaxies in groups with masses lower than 10^{12}M$_\odot$ distinctly increases, as seen from Figure 17. Pereyra et al. (2020) obtained similar results with dark matter velocity field. In general, outside galaxies in the same mass range have a decreasing velocity as the distance from the filament grows. The filament radius divides these galaxies into different regions defined by velocity gradient. On the outside, galaxies accelerate towards filaments. The decreasing velocities inside of filaments can be explained through the number density of central

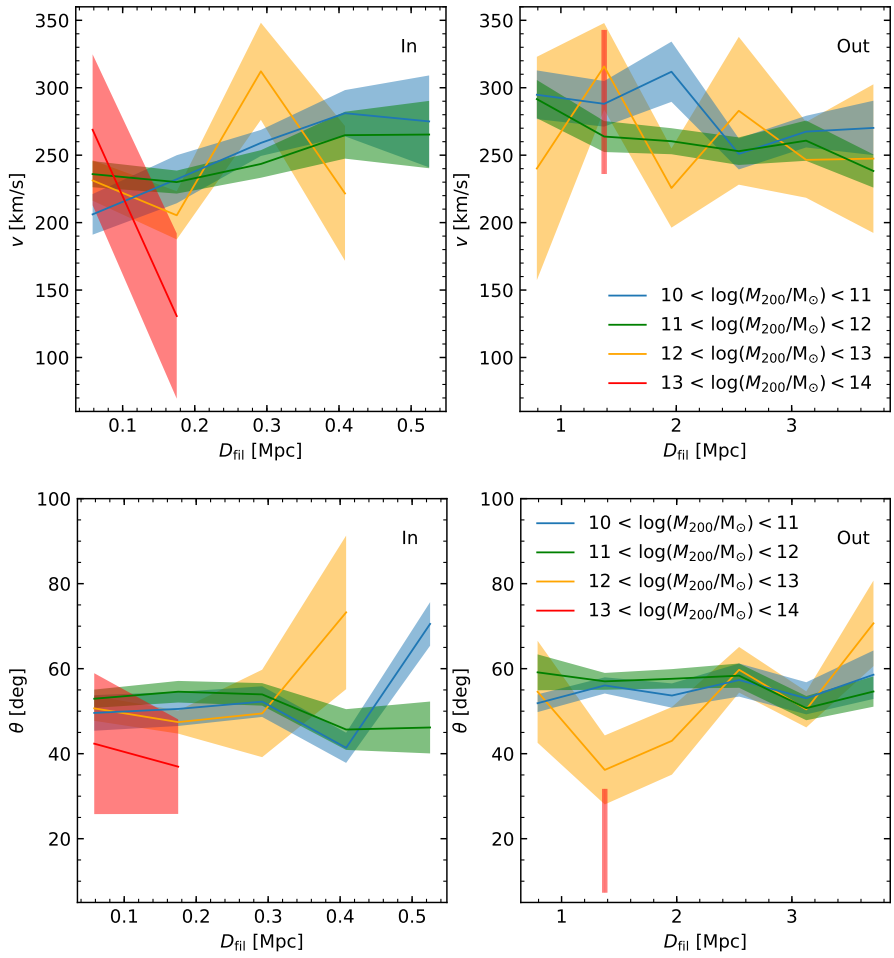

Figure 17: Top panel: the median peculiar velocity of central galaxies as a function of perpendicular distance inside (left) and outside (right) of filaments. Bottom panel: the median alignment angle of central galaxies as a function of perpendicular distance inside (left) and outside (right) of filaments. Central galaxies are shown with fixed group halo mass.

galaxies as a function of the perpendicular distance, shown in Figure 18. The galaxies are clearly concentrated near the filament spines. Beyond the median filament radius $R_{\rm fil} \sim 0.6$ Mpc the galaxy number densities drop significantly and follow almost a constant value out to 4 Mpc. The increase in galaxy number densities inside of filaments with decreasing perpendicular distance leads to increased rate of interactions, possibly slowing down the galaxies by the same mechanics that partly cause the alignment of galaxy spins. The concentration of massive groups near the spines seen in Figure 17 is in accordance with observations of galaxy masses increasing

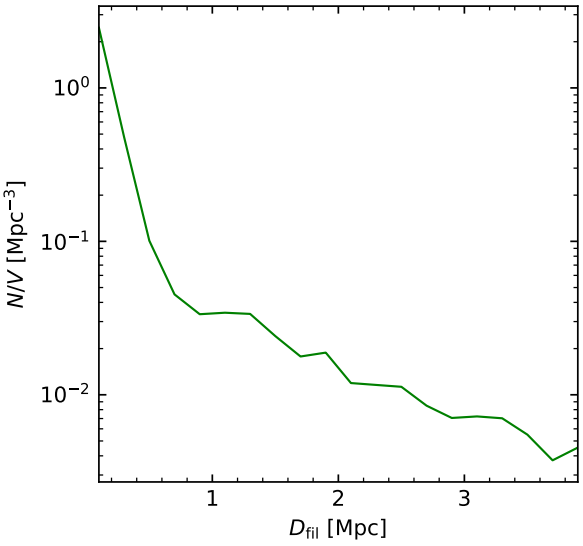

Figure 18: The median density profile inside and around of filaments measured from central galaxy counts as a function of the perpendicular distance from the filament spines.

towards the filament spines (Laigle et al. 2018; Sarron et al. 2019).

Both inside and outside of filaments, the direction of peculiar motions are quite constant with the perpendicular distance and independent of group mass, except for the perpendicular alignments of filament galaxies in the mass range $10^{10-11}\mathrm{M}_\odot$ and $10^{12-13}\mathrm{M}_\odot$, and the parallel alignments of the outside galaxies near the filament edges in the mass range $10^{12-14}\mathrm{M}_\odot$. These alignments and the velocities of filament galaxies in the mass range $10^{12-14}\mathrm{M}_\odot$ could be due to local interactions. It should be noted that each perpendicular distance bin contains galaxies in a cylindrical volume over the whole filament length. This could efficiently average out some trends caused by the filament saddle points. Still, the alignment angles of galaxies in the mass range $10^{10-12}\mathrm{M}_\odot$ are shown to be more perpendicular on the outside of the filaments.

The normalised perpendicular distance in Figure 19 shows a similar increasing trend in the velocities of filament central galaxies in groups with masses below $10^{12}\mathrm{M}_\odot$ as Figure 17, with the decrease in velocities on the outside. The alignment angles are also very similar. The similarity can be expected as stacking the filaments

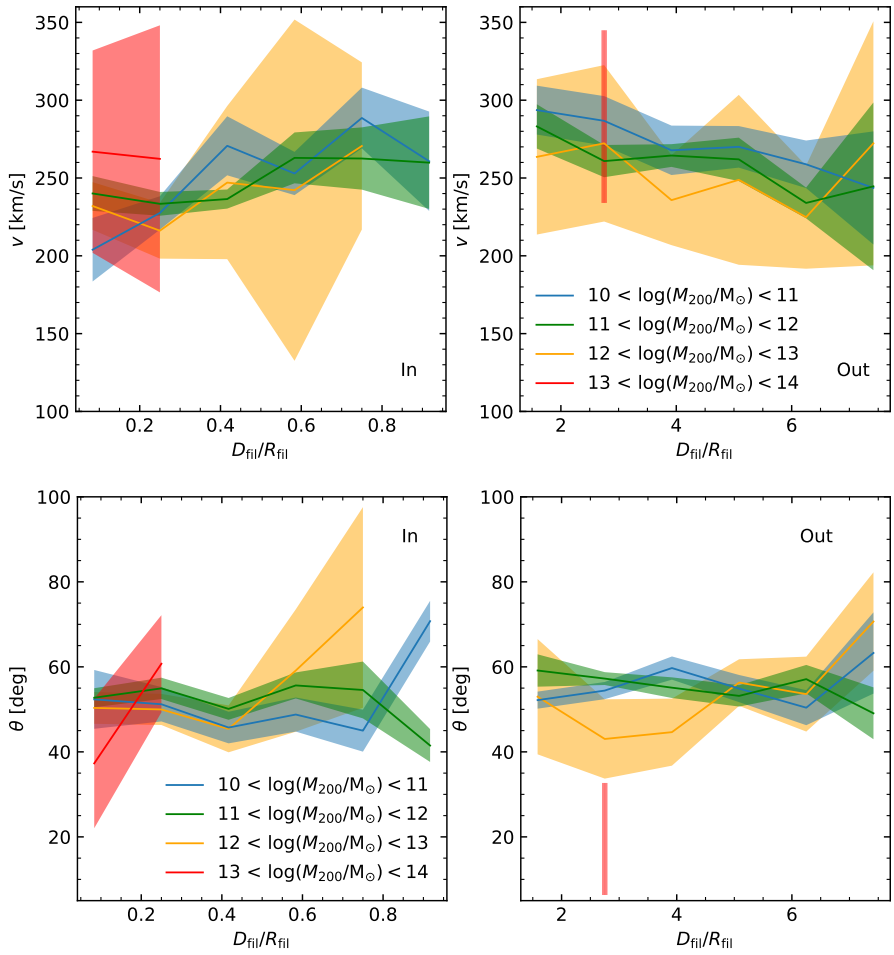

Figure 19: Top panel: the median peculiar velocity of central galaxies as a function of normalised perpendicular distance inside (left) and outside (right) of filaments. Bottom panel: the median alignment angle of central galaxies as a function of normalised perpendicular distance inside (left) and outside (right) of filaments. Central galaxies are shown with fixed group halo mass.

together in the perpendicular direction hides the flow patterns caused by the filament saddle points seen in the parallel direction.

4.4 Peculiar motions and galaxy properties

Galaxy properties are known to correlate tightly with the host halo mass (Behroozi et al. 2010; Weinmann et al. 2006; Wilman & Erwin 2012). The above analysis in this thesis has shown that also the peculiar motions of central galaxies seem to

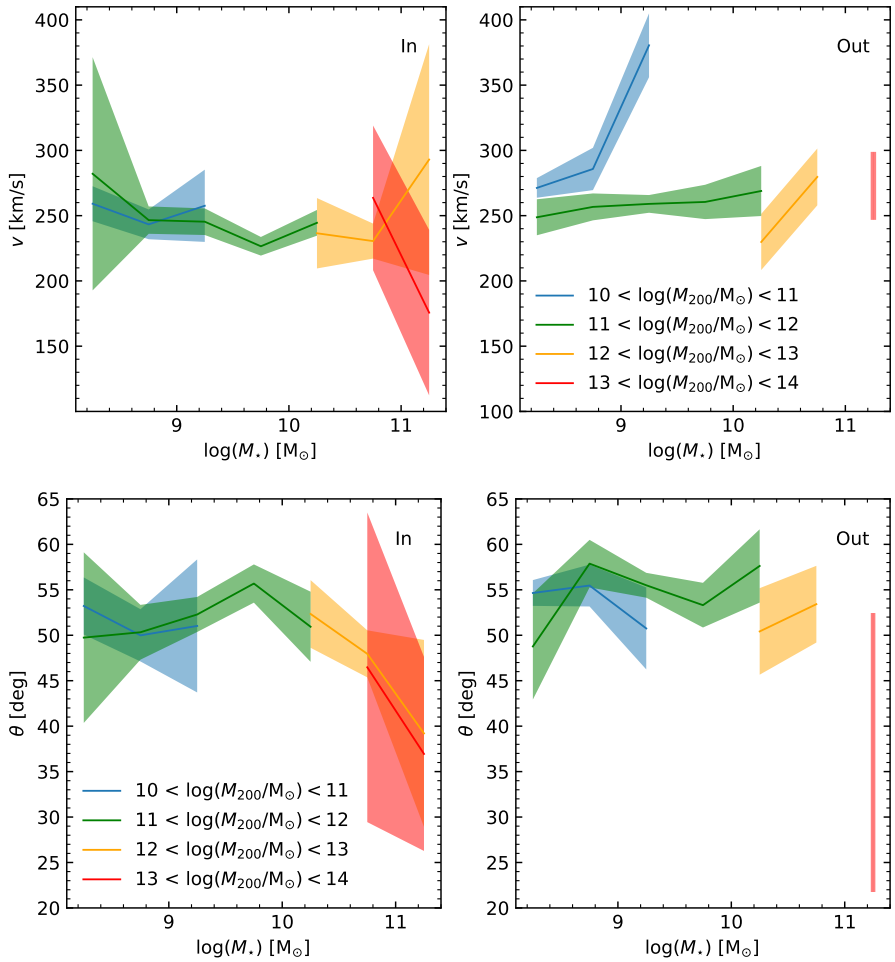

Figure 20: Top panel: the median peculiar velocity of central galaxies as a function of stellar mass inside (left) and outside (right) of filaments. Bottom panel: the median alignment angle of central galaxies as a function of stellar mass inside (left) and outside (right) of filaments. Central galaxies are shown with fixed group halo mass.

be dependent on the mass of the host halo. Finally, in this section the relations between the peculiar motions of central galaxies within the filaments and the galaxy properties are studied. The group mass is fixed in the same way as in the previous sections. The galaxy properties used from the EAGLE simulation are the stellar mass and star formation rate within a 30 kpc aperture, age and color.

Figure 20 shows the peculiar velocities and alignment angles of galaxies as a function of the galaxy stellar mass. It is evident that the stellar mass has no or little effect on the peculiar motions, as any differences both in the velocities and

alignments are mostly due to the group mass. On the outside of the filaments, the galaxies in the low mass groups have increasing velocities with the stellar mass, which is likely due to local streaming.

Although in general the stellar mass depends on the group mass, groups with fixed mass can inhabit galaxies with different stellar masses due to unique assembly histories (Artale et al. 2018). The results obtained in this thesis suggest that the peculiar motions could depend on the halo mass through the experienced interactions. Thus, the uncorrelation between the peculiar motions and stellar masses could indicate that the formation history of halos affects the dynamical and baryonic properties of galaxies in different ways.

Figure 21 shows the peculiar velocities and alignment angles of galaxies as a function of the galaxy age. In the EAGLE simulations the galaxy age is defined as the mean age of stars, weighted by birth mass,

$$\text{Age} = \frac{\sum_i m_i(t - t_i)}{\sum_i m_i}, \tag{34}$$

where t is the age of the universe, t_i is the formation time and m_i is the birth mass of a star particle. The figure shows the same effect that is seen with the stellar masses. Galaxies with fixed group mass can have different ages, but the velocities and alignments do not change much except between different group masses. The figure also shows how a part of the oldest galaxies are located in the most massive groups and have motions parallel with the filament spines. Outside of filaments there is a small set of galaxies in the low mass groups that are very old and have a large dispersion in the velocities. These galaxies are probably accreted from deep void environments and managed to avoid any major interactions.

The galaxy colors are defined as the difference between the dust corrected magnitudes in the g- and r-band. Red and blue galaxies are separated by the value 0.7, red galaxies having $g - r \geq 0.7$ (Einasto et al. 2014). The galaxy peculiar motions as a function of the galaxy colors (Figure 22) shows the same trend as the the stellar

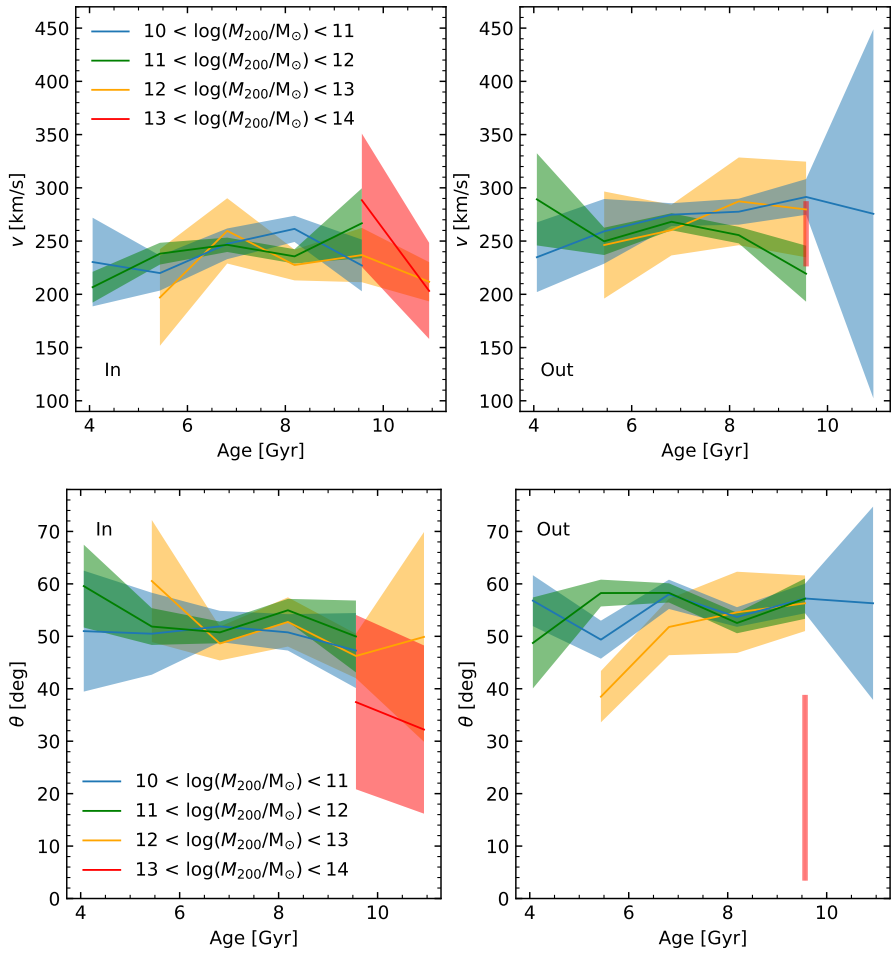

Figure 21: Top panel: the median peculiar velocity of central galaxies as a function of age inside (left) and outside (right) of filaments. Bottom panel: the median alignment angle of central galaxies as a function of age inside (left) and outside (right) of filaments. Central galaxies are shown with fixed group halo mass.

mass and age. In general, all the differences are due to the group mass. However, there is both inside and outside of filaments a large amount of red galaxies in the low mass groups with velocities higher than on the average.

Figure 23 shows the galaxy peculiar velocities and the alignment angles as a function of the galaxy star formation rate (SFR). In general, the galaxy velocities and alignments are constant within errors over the whole range. This could be expected as the other galaxy properties connected to the star formation studied above show no effect on the peculiar motions. Only the motions of filament galaxies

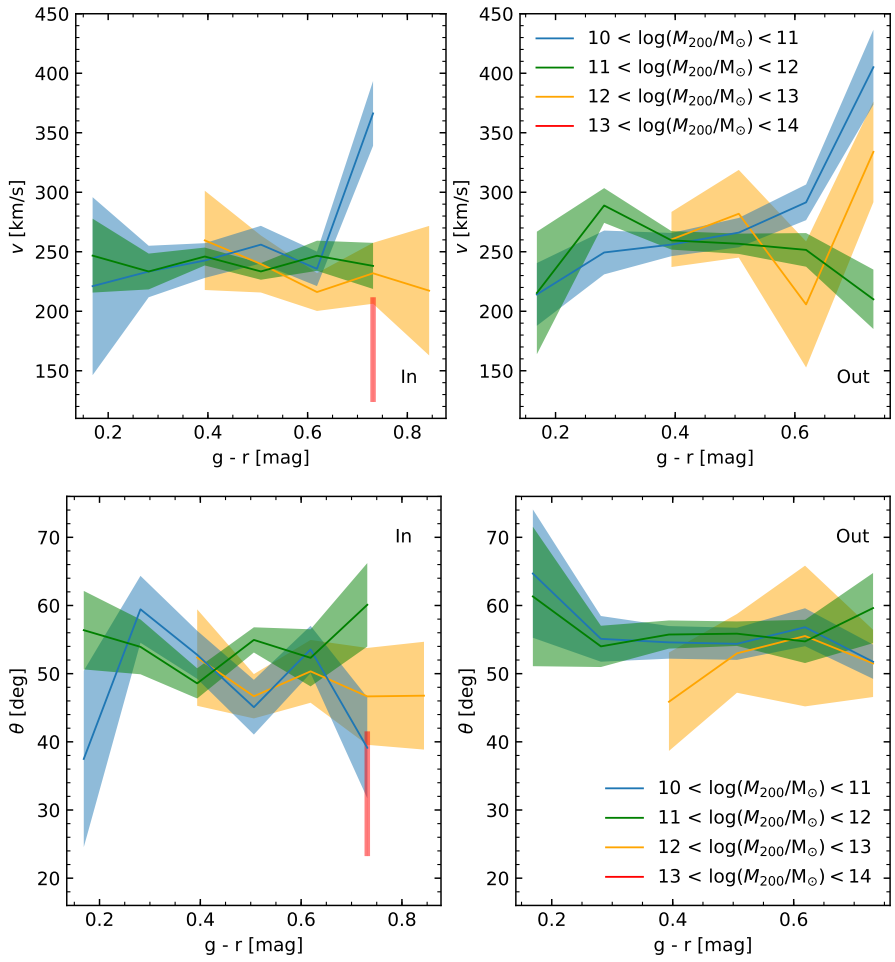

Figure 22: Top panel: the median peculiar velocity of central galaxies as a function of color inside (left) and outside (right) of filaments. Bottom panel: the median alignment angle of central galaxies as a function of color inside (left) and outside (right) of filaments. Central galaxies are shown with fixed group halo mass.

in the mass range $10^{11-12}\mathrm{M}_{\odot}$ show some correlation with the star formation rate. At very low star formation rates, these galaxies have higher velocities and more parallel alignments than on average. This could be again the effect of locally induced flows. Further analysis of the nearby environment would be needed to see the reason behind these motions.

For some of the central galaxies studied in this thesis the EAGLE database does not provide a value for the star formation rate. For most of the galaxies with irregular peculiar motions as a function of galaxy properties and pointed out above,

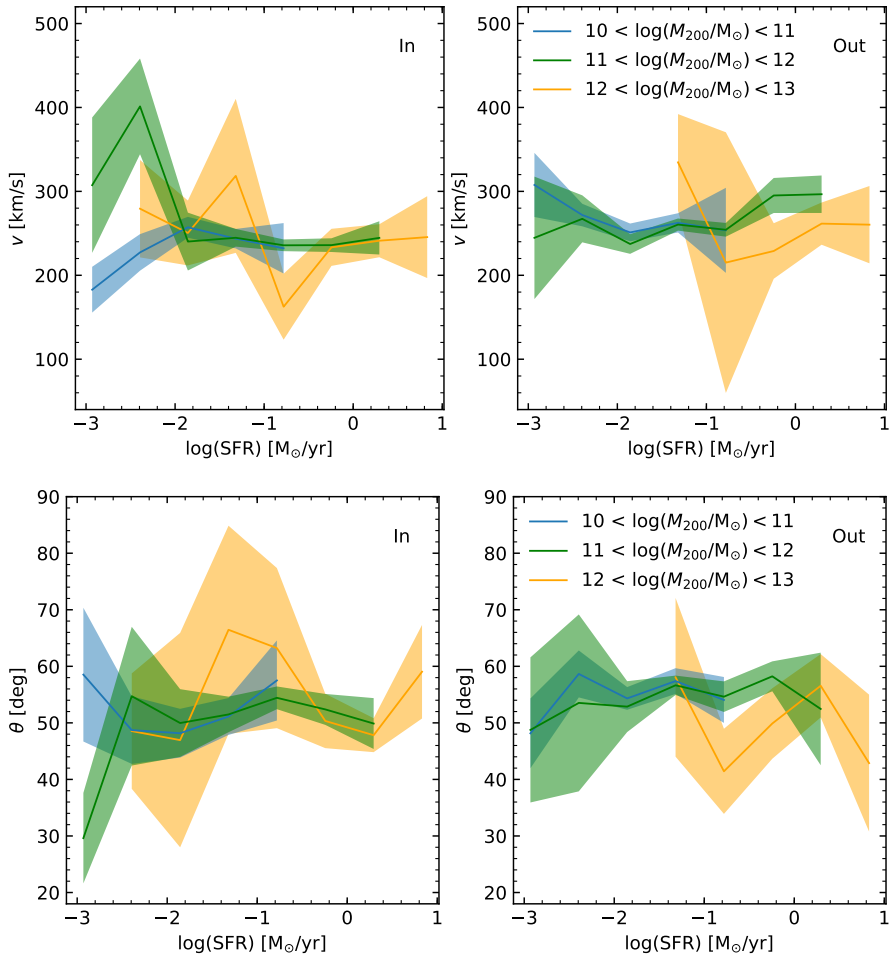

Figure 23: Top panel: the median peculiar velocity of central galaxies as a function of star formation rate inside (left) and outside (right) of filaments. Bottom panel: the median alignment angle of central galaxies as a function of star formation rate inside (left) and outside (right) of filaments. Central galaxies are shown with fixed group halo mass.

there is no value available for the SFR. Apart from these galaxies with no values for the star formation rate, the galaxy properties seem to have no effect on the peculiar motions. This could suggest that the assembly histories of halos affects differently the dynamical and baryonic properties of galaxies.

5 Conclusions and outlook

In this thesis the effect of the filament environment on the central galaxy peculiar motions was studied. To answer the questions presented at the beginning of the analysis, the peculiar motions were compared inside and outside of filaments and measured as a function of geometric properties of filaments and baryonic properties of galaxies. The main results from the analysis are the following.

- Inside of filaments, the peculiar motions of central galaxies differ from those on the outside. The central galaxies generally move more slowly inside of filaments and the motions are more aligned with the filament spines than on the outside of filaments.

It is possible that the decrease in velocities seen inside of filaments is due to that part of the kinetic energy of the central galaxies is converted into the angular momentum of the galaxies by the increased rate of interactions inside of filaments, as filaments are generally denser environments than the surroundings. This is also seen in the decrease of the central galaxy peculiar velocities with increasing group mass both inside and outside of filaments, as more massive groups have generally undergone more major mergers. The central galaxies inside of filaments are likely to be more aligned with the filament spines as they flow towards the clusters at the endpoints of the filaments, while the central galaxies on the outside fall towards the clusters but also the filaments. The central galaxies inside of the most massive groups are the most aligned with the filament spines, as being one of the oldest galaxies they have had the most time to adjust to the flow towards the cluster regions.

- The peculiar motions of galaxies depend on the length of the filament, the parallel distance from the filament endpoints and the perpendicular distance from the filament spines.

The filament length of $\sim$ 15 Mpc seems to divide filaments into two groups. Below this limit, the velocities of central galaxies grow and motions are more parallel with the filament spines with decreasing filament length, while above the limit the velocities are higher and motions are more parallel in longer filaments. One way to explain these motions is that the mass of the clusters that the filaments are connected to could increase with both the shortest and longest filaments, suggested by the concentration of massive groups in short filaments. Short filaments could also act as bridges between two clusters, while long filaments could connect to only one massive cluster, suggested by the one filament longer than 30 Mpc in this study, where coherent and clearly parallel flows towards the endpoint cluster have developed.

The central galaxies in groups with the mass range $10^{10-12}\mathrm{M}_{\odot}$ have almost symmetrical motions around the centers of the filaments and along the filament spines, indicating that in general the filaments are connected by two equal sized clusters. With the normalised parallel distance, the central galaxy peculiar motions are more perpendicular to the filament spines at the centers of the filaments, then diverge from this saddle point and become more parallel as adjusting to the flow towards the clusters, while near the endpoints motions change again to more perpendicular as the central galaxies are probably accreted into different parts of the clusters, rather than a head-on collision.

Inside of the filaments, the peculiar velocities of central galaxies in groups with the mass range $10^{10-12}\mathrm{M}_{\odot}$ decrease closer to the filament spines, while on the outside velocities increase towards the filaments. Outside of the filaments, the central galaxies accelerate towards the filaments. On the inside, the central galaxies slow down possibly due to the increase in angular momentum, as the central galaxy number densities increase towards the filament spines, leading to the increased probability of interactions, shown also with the most massive groups concentrating near the filament spines.

These results hint that in the parallel directions, the peculiar motions of central galaxies inside of filaments are determined by the mass of the galaxy clusters at the endpoints of the filaments, while in the perpendicular directions the peculiar motions seem to be the most affected by the increased galaxy number densities inside of filaments.

- The central galaxy stellar mass, age, star formation rate and color have no effect on the peculiar motions.

Though this study has shown that the group mass has an effect on the peculiar motions of central galaxies, likely through the formation history and the amount of experienced interactions, peculiar motions of central galaxies with fixed group mass do not change with the galaxy properties reflecting this evolution. One possible reason behind this could be that the assembly history of halos affects differently the dynamical and baryonic properties of galaxies.

The results of this thesis could be affected by three possible factors. The first is the decision to study the peculiar motions of individual galaxies rather than the bulk flows, which has both advantages and drawbacks. In the galaxy motions the effect of local streams are enhanced and could obscure large scale flow patterns. On the other hand, this enables the study of the galaxy properties and the distribution of galaxies within filaments, information which would be otherwise lost. Secondly, the analysis of this thesis should be repeated with filaments extracted with a different method, such as the DisPerSE or the NEXUS+ (Sousbie 2011; Cautun et al. 2013), to see if the results are independent of the chosen filament detection method. The third is the rather small box size of the EAGLE simulation. This is seen in the low central galaxy counts, especially in the most massive groups, and in the absence of filaments longer than 30 Mpc except for one. To study more the peculiar motions of galaxies or halos inside of long filaments, a larger simulation would be needed, such as the hydrodynamical IllustrisTNG or the dark matter only Millennium-XXL

(Angulo et al. 2012; Pillepich et al. 2018).

Another natural next step to extend this study would be to explore the relations between the alignment of galaxy spin axes and the direction of the galaxy peculiar motions, as well as the magnitude of the angular momentum and the peculiar velocity, as these seem to be tightly connected as the same mechanics could be shaping these properties. Also a study focused on the region where the filaments and clusters intersect would be needed to study more closely how the cluster masses and sizes affect the peculiar motions. This cannot be achieved with the Bisous method, as it is designed to detect filaments.

This thesis has shown that the filament environment shapes the motions of the galaxies they enclose. The filaments can acquire galaxies through the surrounding environments, and further carry them into clusters of galaxies, acting as true cosmic highways.

References

Alpaslan M., Robotham A. S. G., Driver S., et al., 2014a, MNRAS, 438, 177

Alpaslan M., Robotham A. S. G., Obreschkow D., et al., 2014b, MNRAS, 440, L106

Angulo R. E., Springel V., White S. D. M., et al., 2012, MNRAS, 426, 2046

Aragón-Calvo M. A., 2019, MNRAS, 484, 5771

Aragón-Calvo M. A., Jones B. J. T., van de Weygaert R., van der Hulst J. M., 2007, A&A, 474, 315

Aragón-Calvo M. A., Neyrinck M. C., Silk J., 2019, The Open Journal of Astrophysics, 2, 7

Aragón-Calvo M. A., van de Weygaert R., Jones B. J. T., 2010, MNRAS, 408, 2163

Artale M. C., Zehavi I., Contreras S., Norberg P., 2018, MNRAS, 480, 3978

Barnes J., Hut P., 1986, Nature, 324, 446

Batuski D. J., Burns J. O., 1985, ApJ, 299, 5

Barrow J. D., Bhavsar S. P., Sonoda D. H., 1985, MNRAS, 216, 17

Baugh C. M., Gaztanaga E., Efstathiou G., 1995, MNRAS, 274, 1049

Behroozi P. S., Conroy C., Wechsler R. H., 2010, ApJ, 717, 379

Bond J. R., Kofman L., Pogosyan D., 1996, Nature, 380, 603

Bos E. G. P., van de Weygaert R., Dolag K., Pettorino V., 2012, MNRAS, 426, 440

Brouwer M. M., Cacciato M., Dvornik A., et al., 2016, MNRAS, 462, 4451

Cautun M., van de Weygaert R., Jones B. J. T., 2013, MNRAS, 429, 1286

Cautun M., van de Weygaert R., Jones B. J. T., Frenk C. S., 2014, MNRAS, 441, 2923

Colberg J. M., Krughoff K. S., Connolly A. J., 2005, MNRAS, 359, 272

Colless M., Peterson B. A., Jackson C., et al., 2003, ArXiv e-prints, arXiv:astro-ph/0306581

Crone Odekon M., Hallenbeck G., Haynes M. P., et al., 2018, ApJ, 852, 142

Davis M., Efstathiou G., Frenk C. S., White S. D. M., 1985, ApJ, 292, 371

Dolag K., Borgani S., Murante G., Springel V., 2009, MNRAS, 399, 497

Doroshkevich A. G., 1970, Astrophysics, 6, 320

Dressler A., 1980, ApJ, 236, 351

Eardley E., Peacock J. A., McNaught-Roberts T., et al., 2015, MNRAS, 448, 3665

Ebeling H., Barrett E., Donovan D., 2004, ApJ, 609, L49

Einasto M., Lietzen H., Tempel E., et al., 2014, A&A, 562, A87

Einasto M., Liivamägi L. J., Tempel E., et al., 2012, A&A, 542, A36

Falck B., Neyrinck M. C., Szalay A. S., 2012, ApJ, 754, 126

Falck B., Neyrinck M. C., 2015, MNRAS, 450, 3239

Fixsen D. J., Cheng E. S., Gales J. M., et al., 1996, ApJ, 473, 576

Forero-Romero J. E., Contreras S., Padilla N., 2014, MNRAS, 443, 1090

Ganeshaiah Veena P., Cautun M., van de Weygaert R., et al., 2018, MNRAS, 481, 414

Ganeshaiah Veena P., Cautun M., Tempel E., et al., 2019, MNRAS, 487, 1607

Gao L., Springel V., White S. D. M., 2005, MNRAS, 363, L66

Gingold R. A., Monaghan J. J., 1977, MNRAS, 181, 375

Goh T., Primack J., Lee C. T., et al., 2019, MNRAS, 483, 2101

Gott III J. R., Jurić M., Schlegel D., et al., 2005, ApJ, 624, 463

Hahn O., Porciani C., Carollo C. M., Dekel A., 2007, MNRAS, 375, 489

Haynes M. P., Giovanelli R., 1986, ApJ, 306, L55

Hirv A., Pelt J., Saar E., et al., 2017, A&A, 599, A31

Hockney R. W., Eastwood J. W., 1981, Computer Simulation Using Particles, New York, McGraw-Hill

Hoyle, F. 1949, MNRAS, 109, 365

Hoffman Y., Metuki O., Yepes G., et al., 2012, MNRAS, 425, 2049

Jenkins A., 2010, MNRAS, 403, 1859

Jõeveer M., Einasto J., 1978, IAUS, 79, 241

Knebe A., Gill S. P. D., Gibson B. K., et al., 2004, ApJ, 603, 7

Kraljic K., Pichon C., Dubois Y., et al., 2019, MNRAS, 483, 3227

Kuutma T., Poudel A., Einasto M., et al., 2020, A&A, 639, A71

Kuutma T., Tamm A., Tempel E., 2017, A&A, 600, L6

Laigle C., Pichon C., Arnouts S., et al., 2018, MNRAS, 474, 5437

Libeskind N. I., van de Weygaert R., Cautun M., et al., 2018, MNRAS, 473, 1195

Lietzen H., Tempel E., Heinämäki P., et al., 2012, A&A, 545, A104

Lietzen H., Tempel E., Liivamägi L. J., et al., 2016, A&A, 588, L4

Lin C. C., Mestel L., Shu F. H., 1965, ApJ, 142, 1431

Lucy L. B., 1977, AJ, 82, 1013

Luparello H. E., Lares M., Paz D., et al., 2015, MNRAS, 448, 1483

Lynden-Bell D., Faber S. M., Burstein D., et al., 1988, ApJ, 326, 19

Mo H., van den Bosch F., White S., Galaxy Formation and Evolution, 2010, Cambridge University Press

Peebles P. J. E., 1969, ApJ, 155, 393

Peebles P. J. E., 1980, The large-scale structure of the universe, Princeton University Press

Pereyra L. A., Sgró M. A., Merchán M. E., et al., 2020, MNRAS, 499, 4876

Perlmutter S., Aldering G., Goldhaber G., et al., 1999, ApJ, 517, 565

Pillepich A., Springel V., Nelson D., et al., 2018, MNRAS, 473, 4077

Planck Collaboration et al., 2014, A&A, 571, A16

Platen E., van de Weygaert R., Jones B. J. T., 2007, MNRAS, 380, 551

Pomarède, D., Tully, R. B., Graziani, R., et al., 2020, ApJ, 897, 133

Poudel A., Heinämäki P., Tempel E., et al., 2017, A&A, 597, A86

Riess A. G., Filippenko A. V., Challis P., et al., 1998, AJ, 116, 1009

Rost A., Stasyszyn F., Pereyra L., Martínez H. J., 2020, MNRAS, 493, 1936

Press W. H., Schechter P., 1974, ApJ, 187, 425

Sarron F., Adami C., Durret F., Laigle C., 2019, A&A, 632, A49

Schaye J., Crain R. A., Bower R. G., et al., 2015, MNRAS, 446, 521

Schneider P., Extragalactic Astronomy and Cosmology, An Introduction, 2006, Springer

Shandarin S. F., 2011, J. Cosmology Astropart. Phys., 5, 15

Shandarin S. F., Zel'dovich Y. B., 1989, Reviews of Modern Physics, 61, 185

Sousbie T., 2011, MNRAS, 414, 350

Sousbie T., Pichon C., Colombi S., et al., 2008, MNRAS, 383, 1655

Springel V., 2005, MNRAS, 364, 1105

Springel V., White S. D. M., Tormen G., Kauffmann G., 2001, MNRAS, 328, 726

Stoica R. S., Gregori P., Mateu J., 2005, Stoch. Process. Appl., 115, 1860

Struble, M. F., Rood, H. J. 1999, ApJS, 125, 35

Suhhonenko I., Gramann M., 2003, MNRAS, 339, 271

Tempel E., Guo Q., Kipper R., Libeskind N. I., 2015, MNRAS, 450, 2727

Tempel E., Libeskind N. I., 2013, ApJ, 775, L42

Tempel E., Libeskind N. I., Hoffman Y., et al., 2014a, MNRAS, 437, L11

Tempel E., Stoica R. S., Kipper R., Saar E., 2016, Astron. Comput., 16, 17

Tempel E., Stoica R.S., Martínez V. J., et al., 2014b. MNRAS 438, 3465

Tempel E., Stoica R. S., Saar E., 2013, MNRAS, 428, 1827

Tempel E., Tamm A., 2015, A&A, 576, L5

Trowland H. E., Lewis G. F., Bland-Hawthorn J., 2012,ApJ, 762, 72

Tully R. B., Courtois H. M., Dolphin A. E., et al., 2013, AJ, 146, 86

Tully R. B., Courtois H., Hoffman Y., Pomarède D., 2014, Nature, 513, 71

Tully, R. B., Fisher, J. R., 1987, Nearby galaxies Atlas, Cambridge University Press

Tuominen T., Nevalainen J., Tempel E., et al., 2021, A&A, 646, A156

van der Marel R. P., Besla G., Cox T. J., et al., 2012, ApJ, 753, 9

van de Weygaert R., Schaap W., 2009, Lect. Notes Phys. 665, 291

van Haarlem M., van de Weygaert R., 1993, ApJ, 418, 544

Vogelsberger M., Marinacci F., Torrey P., Puchwein E., 2020, Nature Reviews Physics, 2, 42

Vulcani B., Poggianti B. M., Moretti A., et al., 2019, MNRAS, 487, 2278

Weinmann S. M., van den Bosch F. C., Yang X., Mo H. J., 2006, MNRAS, 366, 2

Wilman D. J., Erwin P., 2012, ApJ, 746, 160

Zel'Dovich Y. B., 1970, A&A, 500, 13

Zel'dovich Y. B., Einasto J., Shandarin S. F., 1982, Nature, 300, 407